

Compton Form Factor Extraction using Quantum Deep Neural Networks

Brandon B. Le^{1,*} and D. Keller^{1,†}

¹*Department of Physics, University of Virginia, Charlottesville, VA 22904, USA.*

(Dated: July 30, 2025)

We present an extraction of Compton Form Factors (CFFs) from Deeply Virtual Compton Scattering (DVCS) experiments conducted at Thomas Jefferson National Accelerator Facility, utilizing Quantum Deep Neural Networks (QDNNs). The analysis employs the standard Belitsky, Kirchner, and Müller formalism at twist-two, complemented by a fitting procedure designed to minimize model dependence in a manner analogous to conventional local fits. A pseudodata extraction test of the CFFs is performed using both Classical Deep Neural Networks (CDNNs) and QDNNs, with a detailed comparative analysis. Results indicate that QDNNs can outperform CDNNs in particular cases, offering enhanced predictive accuracy and precision even with limited model complexity. Motivated by this, we develop a metric to quantify the extent of the quantum advantage based on characteristics of DVCS experimental data. These findings underscore the promising role of QDNNs in advancing future investigations into multidimensional parton distributions and hadronic physics.

CONTENTS

I. Introduction	1
II. Theory Framework	4
III. Quantum Deep Neural Networks	6
A. Quantum Classification	8
1. Quantum Classifier Example	10
B. Quantum Regression	12
1. Quantum Regression Example	12
2. Quantum Qualifier	14
IV. Experimental Data and Pseudodata Generation	16
A. Pseudodata Generation	16
V. Pseudodata CFF Extraction	17
A. Basic QDNN	18
1. Model Complexity	18
2. CFF Extraction Test	19
B. Leveraging the Quantum Advantage	22
1. Full QDNN Model	22
2. CFF Extraction Results	22
VI. DVCS Quantum Qualifier	24
A. Pseudodata Generation	24
B. Quantum Qualifier	24
VII. Optimized CFF Extraction from Experimental Data	25
A. Realistic Pseudodata Generation	26
B. Realistic Pseudodata Extraction	26
C. Experimental Data Extraction	27
VIII. Conclusion	29

Acknowledgments

A. Additional Information	30
1. Regression Target Functions	30
2. Improved QDNN Models	30
3. Tables	30
References	35

I. INTRODUCTION

Exploring the internal structure of the nucleon has been a longstanding goal in hadronic physics, with deeply virtual exclusive processes providing a crucial window into its partonic composition. Among these, Deeply Virtual Compton Scattering (DVCS) stands out as a uniquely sensitive probe of Generalized Parton Distributions (GPDs), which encode the spatial and momentum distributions of quarks and gluons. By linking longitudinal momentum fractions to transverse spatial coordinates, GPDs provide critical insights into the orbital angular momentum carried by partons, bridging the gap between experimental observables and the deeper theoretical understanding of nucleon structure.

Despite their fundamental importance, GPDs cannot be directly extracted from experimental measurements due to their integral appearance in DVCS amplitudes. Instead, Compton Form Factors (CFFs) emerge as a more experimentally accessible alternative, encapsulating the convolution of GPDs with perturbative coefficient functions. These complex-valued functions serve as indirect yet powerful observables, enabling the study of quark and gluon distributions through measurable quantities such as cross sections and asymmetries. This may necessitate the advancement of analysis techniques to go beyond classical methods, leveraging approaches capable of capturing the quantum correlations inherent in the DVCS process. In this context, quantum deep neural networks (QDNNs) offer a promising approach to the systematic extraction of quantum information pertaining to partonic

* sxh3qf@virginia.edu

† dustin@virginia.edu

degrees of freedom, enhancing our ability to measure and interpret the internal quantum structure of the nucleon.

QDNNs are neural network architectures that take advantage of quantum mechanics to process information. Unlike classical deep learning models that rely on traditional computation, QDNNs employ quantum circuits as trainable components, allowing them to explore complex, high-dimensional function spaces more efficiently. Libraries such as PennyLane and Quantum TensorFlow provide frameworks to construct and train QDNNs using hybrid quantum-classical approaches. These frameworks enable the encoding of classical or quantum data into quantum states, allowing manipulation through quantum circuits, and extraction of results via measurement processes. PennyLane is designed to integrate quantum computing with machine learning and automatic differentiation techniques, allowing users to build quantum nodes (or “QNodes”) that can be optimized in conjunction with classical deep learning architectures. Quantum TensorFlow extends Google’s TensorFlow to incorporate quantum computation, enabling quantum variational circuits to be trained using classical gradient descent methods. These tools provide a seamless way to incorporate quantum algorithms into machine learning tasks, facilitating the study of quantum-enhanced feature extraction, pattern recognition, and regression tasks, particularly those of a quantum nature.

One application of QDNNs is in the extraction of kinematically sensitive parameters, such as Compton Form Factors (CFFs), from helicity amplitudes in deeply virtual Compton scattering (DVCS). In DVCS, the helicity amplitudes encode critical information about the nucleon’s partonic structure, represented as complex-valued functions of kinematic variables like momentum transfer squared t , Bjorken scaling variable x_B , and photon virtuality Q^2 . Extracting CFFs from experimental data is challenging due to limited constraints and the interference with the Bethe-Heitler process, where the final state (electron, nucleon, and photon) arises from two coherent quantum amplitudes that interfere constructively or destructively. This interference, driven by quantum superposition and phase coherence, complicates the separation of DVCS contributions. Traditionally, feed-forward deep neural networks have been used to fit experimental data and extract these parameters. However, classical models may struggle to efficiently capture the complex quantum correlations [1] and interference patterns inherent in the data, especially if the data has large experimental errors. QDNNs offer a novel approach by encoding kinematic inputs into quantum states and processing them with quantum variational circuits. While the quantum mechanical properties of QDNNs, such as entanglement in their circuit architecture, are primarily used as a flexible parameterization for regression, they may provide enhanced expressive power [1] to model the intricate structures in DVCS data compared to classical networks under particular circumstances. This potential advantage warrants further exploration to determine whether QDNNs

can better represent the underlying quantum correlations in DVCS processes or simply provide an alternative complementary extraction tool.

The non-perturbative structure of helicity amplitudes in processes like DVCS often involves complex transformations between Generalized Parton Distributions (GPDs), CFFs, and measurable observables. Since QDNNs operate in a Hilbert space, they inherently support the representation of complex-valued functions, making them well-suited for approximating helicity amplitudes. Specifically, quantum feature maps in PennyLane allow one to encode cross-section data into quantum states, which can then be evolved using parameterized quantum circuits to optimize for the best representation of the underlying CFFs. A variational quantum circuit (VQC) can be trained to approximate the mapping between experimental observables, such as beam-spin asymmetries, and the CFFs that define them. This process involves quantum data encoding, where experimental data, including kinematic variables, are transformed into quantum states using amplitude or basis encoding, effectively translating kinematic dependencies into quantum states. The next step is quantum circuit evolution, in which a series of quantum gates parameterized by tunable angles is applied to transform the encoded information. These gates are chosen to represent the functional relationship between helicity amplitudes and observables. Finally, measurement and training are performed by extracting relevant quantities and using hybrid quantum-classical optimization methods, such as quantum natural gradient descent, to adjust the parameters in the quantum circuit to fit the data.

By leveraging quantum entanglement and interference, QDNNs can capture nontrivial correlations between observables that are difficult for classical models to learn efficiently. In CFF extraction, classical extraction techniques have to approximate real and imaginary parts separately, possibly missing quantum interference and correlation effects that are intrinsic to the DVCS amplitude. However, a QDNN can process this information holistically by leveraging superposition and quantum state evolution, which naturally preserve these quantum correlations [1]. Additionally, quantum-enhanced feature spaces allow for a more expressive representation of the functional dependencies of helicity amplitudes. This is particularly useful in scenarios where experimental uncertainties and systematic errors obscure direct parameter extraction. Since QDNNs operate in a higher-dimensional Hilbert space, they can encode more complex functional mappings, potentially leading to more accurate determinations of observables like beam-spin and target-spin asymmetries, which are crucial in probing the nucleon structure.

With the rapid advancement of near-term quantum processors, such as those developed by IBM, Google, and Rigetti, experimental physics stands at the threshold of utilizing QDNNs for real-world data analysis. A promising approach involves integrating quantum machine

learning with Monte Carlo sampling methods to systematically propagate experimental errors through the quantum model, improving the robustness of extracted parameters like CFFs. The application of Quantum DNNs in libraries like PennyLane and Quantum TensorFlow offers a new paradigm for extracting quantum-mechanical observables in nuclear and high-energy physics. By exploiting quantum feature spaces, entanglement, and parameterized quantum circuits, these models can potentially outperform classical approaches in unraveling the helicity structure of deeply virtual processes like DVCS. As quantum hardware continues to improve, QDNNs may soon become indispensable tools for analyzing quantum field-theoretic processes, leading to deeper insights into the fundamental structure of matter. This approach may enhance the extraction fidelity of critical observables and open new avenues for studying the quantum correlations embedded within the hadronic structure.

High-statistics, finely binned data from experimental facilities such as Jefferson Lab have provided insight into the valence quark region, while complementary measurements from HERA and COMPASS have explored the role of sea quarks and gluons in deeply virtual processes. These data sets serve as the basis for generating pseudo-data and set initial benchmarks for developing and validating machine learning techniques, enabling systematic comparisons between CDNNs and QDNNs.

Looking ahead, future experimental programs such as the Electron-Ion Collider (EIC) will dramatically expand the kinematic reach of DVCS measurements, particularly in the sea quark- and gluon-dominated regime. The combination of these new data with advanced QDNN-based extraction techniques offers a powerful opportunity to deepen our understanding of the nucleon's internal structure. By leveraging quantum machine learning to disentangle the intricate relationships between spatial and momentum distributions, these methods could bring us closer to achieving a fully resolved three-dimensional mapping of partonic structure, uncovering new aspects of hadronic physics that remain inaccessible to classical approaches.

In this work, we demonstrate some very basic applications of QDNNs for information extraction and develop some metrics for comparison. Then we perform some extraction testing using a standard local fit that involves fitting a single observable at fixed kinematics, across the independent variable ϕ , the azimuthal angle between the lepton and hadron scattering planes. Local fitting relies on the chosen framework of general approximation, such as twist truncation, leading-order contributions, and the dominance of some CFFs. At the highest approximation, the parametrization of observables, such as the cross section, in terms of CFFs is not unique as it is convention-dependent since it violates the required symmetries, which are restored by contributions that are formally suppressed by powers of $1/Q$, dubbed higher-twist corrections. In this regard, the extracted CFF depends on the choice of the observable formalism [2–7].

While local fits offer the advantage of being potentially model-independent, extracting unique CFFs for fixed kinematics remains a formidable challenge, particularly when the number of available observables is limited, reducing the constraints in the fit. Since CFFs can vary freely within a high-dimensional parameter space, standard χ^2 minimization methods often suffer from inconsistent local minima, leading to significant uncertainties in their extraction, even in the most rigorous analyses. As experimental datasets continue to grow in both quantity and precision, particularly with the inclusion of multiple polarized observables, the issue of data sparsity is gradually improving. However, to fully capitalize on these advances, it is equally crucial to refine and enhance extraction techniques, ensuring that they are capable of handling the increasing complexity and correlations of the data.

We employ a straightforward approach using simple feedforward architectures and, similar to previous work [8, 9], incorporate the helicity amplitude formalism directly into the loss function during the backpropagation of error. To account for experimental uncertainties, we propagate errors through a Monte Carlo ensemble of replicas [10], where the cross section data is resampled within its experimental uncertainty. This ensemble generates a distribution of extracted CFFs, with the width of the distribution reflecting both the inherent experimental errors and the uncertainties arising from the fitting procedure.

We focus on the least constrained observable case: the unpolarized DVCS cross section. We adopt the formalism developed by Belitsky and Müller, specifically the BKM10 framework [4], which defines the structure of the helicity amplitudes used in the extraction. While this approach is tailored to the BKM10 formalism, the extraction method itself is general and can be adapted to alternative theoretical frameworks as needed. Future work will explore an expanded approach aimed at minimizing potential biases introduced by the choice of helicity amplitude formalism. A brief overview of the BKM10 formalism will be provided in the next section.

In this study, we compare the performance of CDNNs and QDNNs in the extraction of CFFs, using a consistent theoretical framework and a new quantum metric. To ensure a direct comparison, we use the BKM10 formalism [4] for both approaches, maintaining uniformity in the helicity amplitude structure used in the loss function. We also focus on quantifying and matching model complexity. By applying identical pseudo input data and theoretical constraints, we systematically evaluate how QDNNs enhance the extraction process relative to CDNNs, particularly in the context of the various contributions to the extraction error and fit ambiguities. The BKM10 formalism, which will be briefly discussed in the next section, provides a well-established foundation for this comparative study, allowing us to isolate the advantages or disadvantages introduced by quantum machine learning techniques.

The remainder of this article is organized as follows. Section II provides a comprehensive overview of the theoretical framework for Deeply Virtual Compton Scattering (DVCS), detailing the role of Compton Form Factors (CFFs) in the extraction process. Section III introduces Quantum Deep Neural Networks (QDNNs), explaining their architecture and advantages over Classical Deep Neural Networks (CDNNs). Examples are provided that explore quantum classification and regression, comparing QDNN and CDNN performance on basic classification and regression tasks with well-defined metrics using pseudodata. Section IV describes the experimental data from Thomas Jefferson National Accelerator Facility used both to generate pseudodata for testing and as input for the extraction of real experimentally determined CFFs in Sec. VII. Section V details the methodology for CFF extraction, including a comparative analysis of CDNN and QDNN performance using accuracy, precision, and error metrics. Section VI develops a DVCS “quantum qualifier,” a metric designed to predict whether a QDNN will outperform a CDNN in CFF extraction based purely on the characteristics of the experimental DVCS data. Section VII applies the optimized QDNN methodology to real experimental DVCS data, showcasing the practical utility and robustness of the quantum approach in a realistic setting. Finally, Sec. VIII discusses the results and concludes with key findings and future research directions for quantum-enhanced parameter extraction in hadronic physics.

II. THEORY FRAMEWORK

To fully appreciate the challenges of extracting CFFs and how quantum models might help, we begin with a review of the theoretical framework that connects GPDs, CFFs, and measurable DVCS observables. The DVCS process studies the virtual Compton scattering in deep-inelastic kinematics at the leading order in perturbative QCD. DVCS is dominated by single-quark scattering, and therefore the amplitude can be expressed in terms of the off-forward parton distributions. In the helicity-independent case, a virtual photon scatters from an unpolarized electron beam of energy k off an unpolarized proton leading to the 4-fold photon electroproduction differential cross section:

$$\frac{d^4\sigma}{dx_B dQ^2 dt |d\phi|} = \frac{\alpha^3 x_B y^2}{8\pi Q^4 \sqrt{1+\epsilon^2}} \frac{1}{e^6} |\mathcal{T}|^2. \quad (1)$$

The phase space of this process is parameterized by the Bjorken variable, $x_B = Q^2/2pq$, the four-momentum $q = k - k'$ carried by the virtual photon of mass $Q^2 = -q^2 = -(k - k')^2$, the squared momentum transfer between the initial and final protons $t = \Delta^2$ with $\Delta = p' - p$ and the lepton energy loss $y = (p \cdot q)/(p \cdot k)$. The azimuthal angle ϕ between the leptonic and hadronic planes is defined in the Trento convention [11]. In the

cross section, $\alpha = e^2/(4\pi)$ is the fine structure constant, and $\epsilon = 2x_B M/Q^2$ where M is the proton mass.

The photon electroproduction cross section is sensitive to the coherent interference of the DVCS amplitude with the Bethe-Heitler (BH) amplitude. The DVCS process, namely, the electroproduction of a photon off a proton with the exchange of a photon with virtuality, Q^2 , much larger than the momentum transfer squared t , hypothetically provides one of the cleanest probes of the GPDs. The BH is an easily calculated electromagnetic process, where a real photon is emitted by the initial or the final lepton. Therefore, both DVCS and BH channels contain the same final states, which can not be distinguished experimentally, and the total cross section arises from the modulus squared of the coherent sum of amplitudes:

$$|\mathcal{T}|^2 = |\mathcal{T}_{DVCS}|^2 + |\mathcal{T}_{BH}|^2 + \mathcal{I}, \quad (2)$$

with the interference term \mathcal{I} being:

$$\mathcal{I} = \mathcal{T}_{DVCS} \mathcal{T}_{BH}^* + \mathcal{T}_{DVCS}^* \mathcal{T}_{BH}. \quad (3)$$

The BH contribution is computed exactly in [2]. It is well known from QED calculations with great precision in terms of the proton electromagnetic form factors in the range of $-t < 0.4 \text{ GeV}^2$ and will not be discussed in detail. The unpolarized BH amplitude is given by:

$$|\mathcal{T}_{BH}|^2 = \frac{e^6}{x_B^2 y^2 (1 + \epsilon^2)^2 t \mathcal{P}_1(\phi) \mathcal{P}_2(\phi)} \sum_{n=0}^2 c_n^{BH} \cos(n\phi). \quad (4)$$

The harmonic terms c_n^{BH} of the BH amplitude squared depend only upon bilinear combinations of the electromagnetic form factors $F_1(t)$ and $F_2(t)$, which are computed from Kelly’s parametrization [12]. The factors $\mathcal{P}_1(\phi)$ and $\mathcal{P}_2(\phi)$ are the electron propagators in the BH amplitude.

The DVCS amplitude encodes the partonic structure of the nucleon given by the Compton tensor $T^{\mu\nu}$ [13] where the observables for the extraction of GPDs emerge. The proven QCD factorization theorem on DVCS [14, 15], permits to express the Compton tensor into perturbative coefficients and the long-distance dynamics that give rise to the GPDs and introduce the handbag diagrams twist expansion. The proven QCD factorization theorem on DVCS [14, 15], which is valid only at values of t such that $-t \ll Q^2$, permits separating the Compton tensor into the hard scattering process at short distances between the virtual photon, electron, and quarks, which can be calculated using perturbative QCD, from the soft, long-distance dynamics that give rise to the non-perturbative GPDs that describe the internal structure of hadrons. The soft interactions of the struck parton by the virtual photon with the rest of the proton can be viewed as the exchange of partons of virtuality of the order of Q^2 . Powers of $1/Q$ suppress their contribution to the cross section of the process as the number of exchanged partons increases. The hard part of scattering processes is described using a perturbative expansion in increasing

orders of the strong coupling constant α_s . This perturbative expression of the hard part in the scattering process is known as the coefficient function.

At leading order (LO) in perturbative QCD and leading twist (LT) approximation, four independent proton GPDs can be accessed in the DVCS process: H , E , \tilde{H} and \tilde{E} . These four GPDs depend on three variables: x , ξ and t where the latter two are experimental parameters with the skewness $\xi = x_B/(2 - x_B)$ at leading twist and $x \pm \xi$ the light-cone longitudinal momentum fraction of the struck quark before (“+” sign) and after (“−” sign) the scattering, such that the difference in the momentum fraction of the quark before absorbing the virtual photon and after the emission of the real photon is given by 2ξ , resulting in a squared four-momentum transfer t to the nucleon. This gives rise to the division of the GPDs into two distinct regions, each carrying entirely different physical interpretations. In the region where the momentum fraction x exceeds ξ or falls below $-\xi$ the GPDs are interpreted as the amplitudes governing the emission and reabsorption of a parton. Conversely, within the region encompassing $-\xi < x < \xi$, GPDs resemble distribution amplitudes governing the emission or absorption of a parton-antiparton pair.

Generalized Parton Distributions (GPDs) arise from the fact that, in the DVCS process, they enter the amplitude through integrals over the parton momentum fraction x spanning the interval $[-1, 1]$, thereby obscuring direct pointwise reconstruction of the GPDs themselves. Since the momentum fraction x is not experimentally accessible, the DVCS cross section is expressed in terms of the CFFs, which are convolution integrals of GPDs over x and are directly accessible through experimental observables via suitable parameterizations. The twist-2 CFFs are weighted integrals of these twist-2 GPDs over x or combinations of GPDs at the line $x = \xi$. The four quark CFFs $\mathcal{F} = \{\mathcal{H}, \mathcal{E}, \tilde{\mathcal{H}}, \tilde{\mathcal{E}}\}$ are related to the quark GPDs $F = \{H, E, \tilde{H}, \tilde{E}\}$ as:

$$\mathcal{F}(\xi, t) \equiv \sum_q \int_{-1}^1 dx C_q^{[\mp]}(x, \xi) F_q(x, \xi, t), \quad (5)$$

where the leading order complex-valued coefficient function related to the hard scattering part [2, 16] is:

$$C_q^{[\mp]} = e_q^2 \left(\frac{1}{\xi - x - i0} \mp \frac{1}{\xi + x - i0} \right), \quad (6)$$

where e_q is the charge of quarks in units of proton charge and the summation runs over all quark flavors q . Using the residue theorem, it is possible to decompose the integral (5) so that each CFF contains two real quantities:

$$\mathcal{F}(\xi, t) = \text{Re}\mathcal{F}(\xi, t) + i\Im\mathcal{F}(\xi, t), \quad (7)$$

where

$$\text{Re}\mathcal{F}(\xi, t) = \sum_q \mathcal{P} \int_0^1 dx \left(\frac{1}{\xi - x} \mp \frac{1}{\xi + x} \right) F_q^{[\mp]}(x, \xi, t), \quad (8)$$

$$\Im\mathcal{F}(\xi, t) = \pi \sum_q F_q^{[\mp]}(\xi, \xi, t). \quad (9)$$

Here, \mathcal{P} denotes the Cauchy principal value and,

$$F_q^{[\mp]}(x, \xi, t) = e_q^2 [F_q(x, \xi, t) \mp F_q(-x, \xi, t)]. \quad (10)$$

The top sign in equations (5)-(10), corresponds to the unpolarized GPDs (H, E) and the bottom sign applies to the polarized GPDs (\tilde{H}, \tilde{E}). Equations (8) and (9) show that observables sensitive to the imaginary part of the CFFs will only contain information along the line $x = \pm\xi$, whereas the real part probes GPD integrals over the momentum fraction x . Given the complicated kinematic dependence of the GPDs, retrieving them from CFFs is therefore a major challenge of the field, known as the deconvolution problem [17]. Thus, the maximum model-independent information which can be extracted from the DVCS reaction at leading twist are 8 CFFs, which depend on two variables, ξ and t , at QCD leading order. There is an additional Q^2 dependence in the CFFs (and in the GPDs) if QCD evolution is taken into account [18].

Our extraction uses the unpolarized beam and unpolarized target cross sections relying on the Belitsky-Kirchner-Müller DVCS formulation (BKM10) [4] and we focus on the case where only twist-2 CFFs enter the cross section. In this case, the squared DVCS amplitude is a bilinear combination of the CFFs contained in the coefficient $\mathcal{C}^{DVCS}(\mathcal{F}, \mathcal{F}^*)$:

$$|\mathcal{T}^{DVCS}|^2 = \frac{e^6}{y^2 Q^2} \left\{ 2 \frac{2 - 2y + y^2 + \frac{\epsilon^2}{2} y^2}{1 + \epsilon^2} \mathcal{C}^{DVCS}(\mathcal{F}, \mathcal{F}^*) \right\}. \quad (11)$$

The DVCS amplitude is contingent on the four complex-valued twist-2 CFFs consisting of two real magnitudes, leading to the emergence of eight distinct CFF parameters. This intricate multiplicity of parameters underscores the complexity involved in their extraction process. A noteworthy aspect in this context is that, under this approximation, the DVCS process lacks dependence on the azimuthal angle. This can be an advantage in the extraction procedure by taking it as a free parameter.

The unpolarized interference term in Eq. (2), is a linear combination of CFFs, with the following harmonic structure:

$$\mathcal{I} = \frac{e^6}{x_B y^3 t \mathcal{P}_1(\phi) \mathcal{P}_2(\phi)} \sum_{n=0}^3 c_n^{\mathcal{I}} \cos(n\phi), \quad (12)$$

where the Fourier coefficients are:

$$c_n^{\mathcal{I}} = C_{++}^n \text{Re} C_{++}^{\mathcal{I}, n}(\mathcal{F}) + C_{0+}^n \text{Re} C_{0+}^{\mathcal{I}, n}(\mathcal{F}_{eff}) + C_{-+}^n \text{Re} C_{-+}^{\mathcal{I}, n}(\mathcal{F}_{\mathcal{T}}). \quad (13)$$

The double helicity-flip gluonic CFFs amplitudes, $C_{-+}^{\mathcal{I}, n}(\mathcal{F}_{\mathcal{T}})$, are formally suppressed by α_s and will be neglected here. $C_{++}^{\mathcal{I}, n}(\mathcal{F})$ and $C_{0+}^{\mathcal{I}, n}(\mathcal{F}_{eff})$ are the helicity-conserving and the helicity-changing amplitudes respectively. The helicity-changing amplitudes also contain the

contribution from twist-3 CFFs implicit in the effective CFFs (\mathcal{F}_{eff}). Thus, we chose a framework where only the helicity-conserving amplitudes are considered, which contain only pure twist-2 CFFs contributions. In this way, we set more constraints on the physics with the same amount of data, giving up to some information at the expense of greater accuracy in the remaining parameters. The helicity-conserving amplitudes are given by:

$$\begin{aligned} \Re C_{++}^{\mathcal{I},n}(\mathcal{F}) &= \Re C^{\mathcal{I}}(\mathcal{F}) + \frac{C_{++}^{V,n}}{C_{++}^n} \Re C^{\mathcal{I},V}(\mathcal{F}) \\ &\quad + \frac{C_{++}^{A,n}}{C_{++}^n} \Re C^{\mathcal{I},A}(\mathcal{F}). \end{aligned} \quad (14)$$

The complete expressions of the kinematic coefficients C_{++}^n , $C_{++}^{V,n}$ and $C_{++}^{A,n}$ are given in [4]. The $C^{\mathcal{I}}$, $C^{\mathcal{I},V}$ and $C^{\mathcal{I},A}$ terms are a linear combination of the CFFs:

$$C^{\mathcal{I}}(\mathcal{F}) = F_1 \mathcal{H} + \xi(F_1 + F_2) \tilde{\mathcal{H}} - \frac{t}{4M^2} F_2 \mathcal{E} \quad (15)$$

$$C^{\mathcal{I},V}(\mathcal{F}) = \frac{x_B}{2 - x_B + x_B \frac{t}{Q^2}} (F_1 + F_2) (\mathcal{H} + \mathcal{E}) \quad (16)$$

$$C^{\mathcal{I},A}(\mathcal{F}) = \frac{x_B}{2 - x_B + x_B \frac{t}{Q^2}} (F_1 + F_2) \tilde{\mathcal{H}} \quad (17)$$

In this specific scenario, the interference cross section becomes reliant solely on three real-valued CFFs: $\Re \mathcal{H}$, $\Re \mathcal{E}$, and $\Re \tilde{\mathcal{H}}$. The real parts of the CFFs $\Re \mathcal{H}$, $\Re \mathcal{E}$, and $\Re \tilde{\mathcal{H}}$ arise from the dispersive integrals of the corresponding GPDs H , E , and \tilde{H} , representing their convolution with the hard scattering kernel. $\Re \mathcal{H}$ dominates the DVCS amplitude for unpolarized targets and reflects the spatial-momentum distribution of unpolarized quarks. $\Re \mathcal{E}$ is sensitive to nucleon helicity-flip and provides access to parton orbital angular momentum via Ji's sum rule. $\Re \tilde{\mathcal{H}}$ encodes the distribution of polarized quarks and governs the longitudinal spin structure, playing a leading role for polarized targets. Additionally, accounting for the constant nature of the pure DVCS cross section in terms of the azimuthal angle, the total number of parameters that need to be extracted is reduced to four. We chose this framework to make the comparison of CDNN and QDNN extractions more direct. The reduction in the parameter count simplifies the extraction process relative to the full eight-parameter scenario, while still preserving the most relevant aspects of the phenomenological information. This simplified parameter space facilitates a more manageable data analysis and modeling, making a more straightforward demonstration of the extraction steps of the essential parameters from experimental data. A separate future paper will investigate directly the quantum advantage in extracting the complex-valued CFFs.

III. QUANTUM DEEP NEURAL NETWORKS

While the theoretical framework briefly described in the preceding section provides the essential tools and conceptual understanding for characterizing nucleon structure through Compton Form Factors, the practical extraction of these quantities from experimental data presents significant computational challenges. The inherent complexities of the DVCS cross section and the intricate dependencies of CFFs on kinematic variables suggest that a variety of algorithms and approaches should be investigated. With this in mind and to pave the way for the possibility of more precise extractions, this section introduces Quantum Deep Neural Networks (QDNNs). We discuss their fundamental architecture, explaining how these networks leverage quantum mechanical principles such as superposition and entanglement to process information, thereby offering a powerful novel paradigm for complex data analysis.

QDNNs integrate principles of quantum mechanics into deep learning architectures, offering a computational framework distinct from CDNNs. While CDNNs process data using weighted sums and nonlinear activation functions in Euclidean space, QDNNs manipulate quantum states in Hilbert space via unitary transformations. PennyLane [19], a quantum computing library, enables the development of these models by integrating quantum circuits—either simulated or executed on quantum hardware—into classical machine learning frameworks. Although the long-term goal is to deploy QDNNs on fault-tolerant quantum processors, current implementations primarily rely on simulators, which serve as an efficient platform for testing and optimizing quantum neural architectures. These approaches offer alternative algorithmic methods that, in some cases, complement classical deep learning.

In a classical neural network, each layer applies a transformation of the form $h = \sigma(Wx + b)$, where W is a weight matrix, b is a bias term, and σ is a nonlinear activation function. In contrast, QDNNs replace these transformations with quantum operations acting on qubits. A system of n qubits exists in a 2^n -dimensional complex Hilbert space, where its quantum state is represented as a superposition of computational basis states,

$$|\psi\rangle = \sum_{i=0}^{2^n-1} c_i |i\rangle, \quad (18)$$

where $c_i \in \mathbb{C}$ are complex probability amplitudes satisfying the normalization condition

$$\sum_{i=0}^{2^n-1} |c_i|^2 = 1. \quad (19)$$

This normalization ensures that the total probability of measuring any basis state sums to unity, preserving the probabilistic interpretation inherent in quantum mechanics. The evolution of the quantum state is governed by

unitary operators, which preserve the norm of the state vector and satisfy the condition,

$$U^\dagger U = I, \quad (20)$$

where U^\dagger is the Hermitian conjugate (conjugate transpose) of U , and I is the identity matrix. The application of a unitary transformation to a quantum state results in

$$|\psi'\rangle = U|\psi\rangle. \quad (21)$$

The unitary operations in a QDNN are represented as matrices $U \in \mathbb{C}^{2^n \times 2^n}$, ensuring that each operation is a valid quantum transformation that preserves inner products and maintains the reversibility required by quantum mechanics. In contrast to classical neural networks, which apply affine transformations followed by nonlinear activation functions, QDNNs process information using sequences of unitary transformations, where each layer consists of a set of parameterized quantum gates.

A simple example of a single-qubit unitary transformation is a rotation about the x -axis, given by the Pauli rotation matrix

$$R_x(\theta) = e^{-i\theta X/2} = \begin{pmatrix} \cos(\theta/2) & -i\sin(\theta/2) \\ -i\sin(\theta/2) & \cos(\theta/2) \end{pmatrix}. \quad (22)$$

Similarly, rotations about the y - and z -axes are defined by

$$R_y(\theta) = e^{-i\theta Y/2}, \quad R_z(\theta) = e^{-i\theta Z/2}. \quad (23)$$

A full quantum circuit is composed of multiple layers of these parameterized unitary transformations, interspersed with entangling gates that introduce correlations between qubits. The final quantum state of a circuit with L layers is expressed as

$$|\psi_{\text{final}}\rangle = U_L U_{L-1} \cdots U_1 |0\rangle^{\otimes n}. \quad (24)$$

Encoding classical data into quantum circuits is a fundamental step in constructing QDNNs. One commonly used encoding technique is angle embedding, where classical input values are mapped to rotation angles of single-qubit gates. Given an input feature x , the encoding is performed via the transformation,

$$R_x(x)|0\rangle = e^{-ixX/2}|0\rangle. \quad (25)$$

Once encoded, additional parameterized unitary gates modify the quantum state based on learnable parameters. The role of entanglement in QDNNs is particularly significant, as it enables the representation of highly non-trivial correlations that classical networks may require exponentially many parameters to approximate. Entanglement is introduced using multi-qubit gates such as the controlled-NOT (CNOT) gate, represented as the unitary matrix

$$\text{CNOT} = \begin{pmatrix} 1 & 0 & 0 & 0 \\ 0 & 1 & 0 & 0 \\ 0 & 0 & 0 & 1 \\ 0 & 0 & 1 & 0 \end{pmatrix}. \quad (26)$$

By incorporating these entangling operations, QDNNs exploit quantum mechanical effects that enhance the expressivity and representational power of the model.

In this paper, we also frequently use PennyLane's Strongly Entangling Layers to construct quantum circuits, which are composed of alternating layers of trainable single-qubit rotations and fixed two-qubit entangling gates. Each layer applies parameterized rotations on each qubit followed by a sequence of two-qubit entanglers (e.g., CNOT gates) that connect each qubit i to qubit $(i + r) \bmod M$, where M is the number of qubits and r is a tunable parameter known as the entanglement range. This structure allows the circuit to explore a rich and expressive subspace of the full Hilbert space while maintaining a manageable number of trainable parameters.

The final step in a QDNN is measurement, which extracts classical information from the quantum state. The measurements correspond to taking the expectation values of Hermitian observables. The expectation value of an observable O for a quantum state $|\psi\rangle$ is computed as

$$\langle O \rangle = \langle \psi | O | \psi \rangle. \quad (27)$$

For Pauli-Z measurements, this simplifies to

$$\langle Z \rangle = \langle \psi | Z | \psi \rangle = |\langle 0 | \psi \rangle|^2 - |\langle 1 | \psi \rangle|^2. \quad (28)$$

These expectation values form the classical outputs of a QDNN, which can be further processed using classical deep learning methods. The full QDNN architecture, therefore, consists of data encoding, a sequence of parameterized unitary transformations, entangling operations, and final measurement.

To train a QDNN, the parameters θ in the quantum gates are optimized to minimize a loss function, typically defined as

$$f(\theta) = \langle \psi(\theta) | O | \psi(\theta) \rangle. \quad (29)$$

Unlike CDNNs, which compute gradients via backpropagation, QDNNs employ the parameter shift rule [20] to estimate derivatives of expectation values. This quantum gradient calculation is given by

$$\frac{d}{d\theta} \langle Z \rangle = \frac{\langle Z(\theta + \pi/2) \rangle - \langle Z(\theta - \pi/2) \rangle}{2}. \quad (30)$$

This ensures that QDNNs can be trained using familiar gradient-based optimization techniques while preserving quantum coherence.

QDNNs offer a compelling advantage over CDNN due to their ability to exploit the exponential dimensionality of quantum state space [21]. A quantum system with n qubits exists in a Hilbert space of dimension 2^n , allowing QDNNs to represent highly complex transformations with far fewer parameters than classical networks, which scale polynomially [22]. Additionally, quantum entanglement enables QDNNs to model intricate correlations that classical networks struggle to capture efficiently [23].

Superposition further enhances expressivity by allowing quantum states to encode multiple computational pathways simultaneously [24].

One of the most promising theoretical advantages of QDNNs is their trainability in high-dimensional spaces [25]. Both CDNNs and QDNNs face optimization challenges in complex landscapes. CDNNs suffer from vanishing gradients [26], where gradients diminish exponentially with network depth, while QDNNs encounter barren plateaus [27], where gradients vanish exponentially as the quantum circuit scales. Quantum circuits, when carefully designed to leverage entanglement, can mitigate barren plateaus, preserving trainability in larger architectures. Quantum kernel methods and variational quantum circuits have demonstrated enhanced learning efficiency for structured data representations compared to classical approaches [23, 28].

Despite these theoretical advantages, practical QDNN implementation faces challenges due to hardware limitations, including noise, decoherence, and limited qubit connectivity. PennyLane facilitates the development of QDNNs by providing a robust framework for hybrid quantum-classical machine learning, enabling direct comparisons between quantum and classical networks. While most PennyLane computations are currently executed on quantum simulators, which explicitly store quantum states as vectors in Hilbert space and evolve them using matrix multiplications, future developments in quantum hardware may enable large-scale deployment of QDNNs on real quantum processors.

As quantum computing technology advances, QDNNs may surpass CDNNs in efficiency and accuracy for specialized tasks. Theoretically, deep quantum circuits with polynomial-depth entangling layers could approximate function classes exponentially faster than classical models [29]. While the realization of quantum advantage in deep learning remains an open question, QDNNs represent a promising avenue for integrating quantum mechanics into artificial intelligence, unlocking new possibilities in optimization, generative modeling, and high-dimensional learning.

Although quantum supremacy in deep learning is still an open question, early results suggest that QDNNs could offer advantages in feature extraction, kernel-based learning, and generative modeling, particularly for problems with complex high-dimensional structure [21, 23, 25, 29, 30]. By simulating quantum networks on classical hardware today, PennyLane provides a crucial testbed for developing quantum-enhanced deep learning architectures. As quantum technology progresses, these simulations will transition to real quantum processors, unlocking new possibilities for machine learning and data processing. For now, QDNNs remain an experimental but promising approach, representing a step toward harnessing the full potential of quantum computing for information extraction in hadronic phenomenology.

In the following subsections, we investigate methods to quantify the quantum advantage of QDNNs over CDNNs

in classification and regression tasks using precise performance metrics. Identifying optimal tools for evaluating these metrics is critical, particularly for information extraction in hadronic physics applications.

A. Quantum Classification

To better understand the differences between a quantum architecture and a classical one, let us consider a basic classifier DNN. In the simplest case, the architecture can be a basic feedforward single hidden layer classifier designed for binary classification tasks, where the input consists of a set of numerical features. It operates through two fully connected layers: the first projects the input into an eight-dimensional space and applies a rectified linear activation function to introduce nonlinearity, enhancing its ability to capture complex patterns. The second layer reduces the dimensionality to a single output, applying a sigmoid activation function to constrain the result within a probability range suitable for classification. This type of model learns by adjusting its internal parameters through gradient-based optimization techniques, typically using methods like stochastic gradient descent or adaptive moment estimation, minimizing a binary cross-entropy loss function. Its compact design makes it computationally efficient and effective for structured data classification tasks that require mapping numerical inputs to distinct categories based on learned patterns.

The neural network is structured to process an 8-dimensional input feature vector, transforming it through a series of weighted linear operations and nonlinear activations to produce a scalar output. The architecture begins with an input layer that accepts the feature vector $x \in \mathbb{R}^8$, which is then processed by a fully connected hidden layer. This hidden layer applies a linear transformation using a weight matrix $W_1 \in \mathbb{R}^{8 \times 8}$ and a bias vector $b_1 \in \mathbb{R}^8$. The result of this linear operation is then passed through a ReLU activation function, which introduces nonlinearity to the model. This step can be expressed as:

$$h = \text{ReLU}(W_1 x + b_1), \quad (31)$$

where the ReLU function operates element-wise and is defined as:

$$\text{ReLU}(z) = \max(0, z). \quad (32)$$

This activation ensures that only positive values are propagated while setting negative values to zero, enabling the network to learn complex representations while maintaining computational efficiency.

The activated hidden representation h is subsequently processed by the output layer, which consists of another fully connected transformation. This layer applies a weight matrix $W_2 \in \mathbb{R}^{8 \times 1}$ and a scalar bias term b_2 to

produce the final output. The computation at this stage is given by:

$$y = \sigma(W_2 h + b_2), \quad (33)$$

where the function $\sigma(x)$ is the sigmoid activation, defined as:

$$\sigma(x) = \frac{1}{1 + e^{-x}}. \quad (34)$$

The sigmoid function maps the output to a range between 0 and 1, making it particularly well-suited for binary classification tasks. The final scalar value y can be interpreted as the probability of belonging to a particular class, allowing for meaningful decision-making based on the network's learned representations. This structured approach, combining linear transformations with nonlinear activations, enables the model to capture complex relationships within the input data while maintaining interpretability and stability in its predictions.

To construct a similar architecture for a QDNN we need to use quantum perceptrons, where each layer is defined by unitary matrices that evolve quantum states. Instead of weighted sums and nonlinear activations, quantum perceptrons use unitary transformations applied to qubits.

QDNNs can process and classify data in ways that CDNNs cannot. The architecture of a QDNN follows a structured approach, beginning with the encoding of classical data into quantum states, followed by a sequence of parameterized unitary transformations, and concluding with quantum measurement to derive the final classification decision.

A typical QDNN starts with a set of input qubits, which encode classical data into a quantum state. In this example, the network utilizes three input qubits, each representing a transformed version of classical data points. The core of the network consists of multiple hidden layers, where each layer applies parameterized unitary transformations. These unitary transformations serve as the quantum equivalent of weight matrices in CDNNs, allowing the system to evolve the quantum state in a structured and trainable manner. Finally, the last layer of the QDNN extracts useful information through quantum measurement, with a single-qubit measurement providing the classification outcome.

Before classical data can be processed within a QDNN, it must first be encoded into a quantum state. Given a classical input x , the encoding process maps the data into a quantum state representation. This transformation ensures that the network can operate within the quantum mechanical framework, leveraging the unique properties of quantum computation such as superposition and entanglement.

The core computational power of a QDNN lies in its quantum perceptron layers. Each layer applies a unitary transformation U to the quantum state, modifying it while preserving coherence. The evolution of the quantum state follows the transformation, $|\psi'\rangle = U|\psi\rangle$, where

U is a unitary matrix satisfying the condition $U^\dagger U = I$, ensuring that the transformation remains reversible. Unlike classical networks, which rely on weight matrices and biases, the QDNN utilizes these unitary operations to manipulate quantum states without losing quantum information.

The architecture incorporates randomized unitary matrices, generated specifically for each perceptron. These transformations act across multiple qubits, introducing quantum correlations that enhance the network's computational capacity beyond classical architectures. Entanglement plays a fundamental role in this process, enabling a form of information encoding and manipulation that is fundamentally different from classical neural networks.

In a multi-qubit system, transformations must be properly structured to maintain coherence and ensure correct processing. Each unitary transformation in a QDNN is tensored with the identity matrix when applied to multiple qubits, ensuring that transformations operate within the appropriate Hilbert space. Mathematically, this is expressed as $U_{\text{layer}} = U_{\text{qubit}} \otimes I$. This tensoring process ensures that unitary transformations are correctly applied in the quantum circuit without disrupting the overall structure of the network. Additionally, swapped operations are implemented to maintain proper qubit ordering within the layered transformations, further reinforcing the structural integrity of the quantum network.

Once the quantum state has evolved through the network's hidden layers, the final step is to extract a classification decision from the quantum system. This is achieved through a measurement operation, where an observable O , such as the Pauli-Z expectation value, is used to collapse the quantum state into a classical probability. The measurement process follows, $\langle O \rangle = \langle \psi_{\text{final}} | O | \psi_{\text{final}} \rangle$. The extracted expectation value serves as the output of the QDNN, which is then mapped to a binary outcome for classification. This final measurement is a critical component of quantum machine learning (QML), as it translates quantum state information back into a form that can be interpreted in the classical world.

CDNNs and QDNNs share fundamental mathematical structures while exhibiting key differences due to their respective foundations in classical and quantum mechanics. One major distinction lies in the nature of transformations. In CDNNs, transformations are affine, expressed as $h = Wx + b$, whereas in QDNNs, transformations are unitary, evolving quantum states as $|\psi'\rangle = U|\psi\rangle$. This difference reflects the constraint that quantum evolution must preserve coherence, a property absent in classical networks. Another significant difference is the source of nonlinearity. CDNNs explicitly incorporate nonlinear activation functions such as ReLU and Sigmoid, enabling the network to model complex patterns. In contrast, QDNNs rely on measurement-induced nonlinearity since quantum evolution itself is inherently linear.

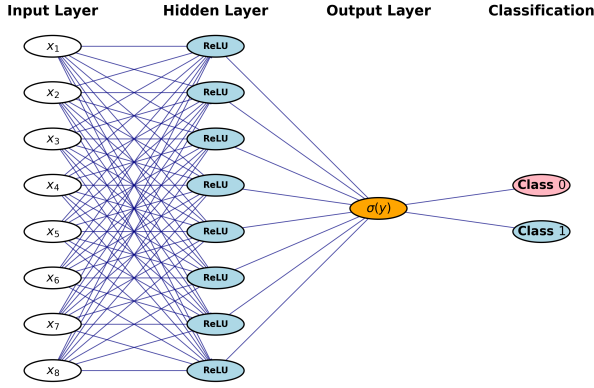


FIG. 1: A schematic representation of a CDNN architecture for binary classification. The input layer consists of 8 features x_i , which are processed through a hidden layer of 8 neurons with ReLU activation. The final output layer consists of a single neuron with a sigmoid activation function $\sigma(y)$, producing a probability score that determines classification into either Class 0 or Class 1.

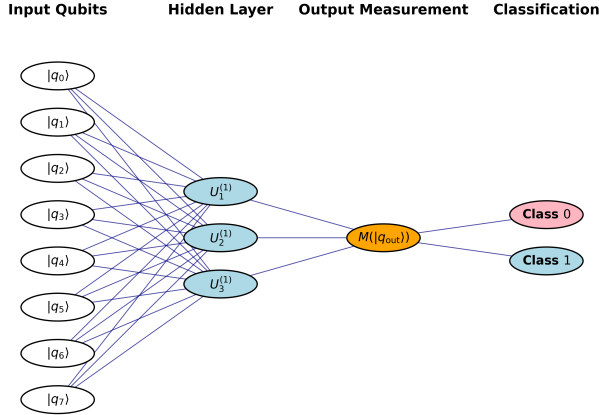


FIG. 2: A schematic representation of a QDNN architecture. The input layer consists of 8 qubits $|q_i\rangle$, which are processed through a hidden layer of quantum perceptrons $U_i^{(1)}$. The final output measurement $M(|q_{out}\rangle)$ determines the classification, assigning the input to either Class 0 or Class 1. The connections represent quantum operations applied between layers.

1. Quantum Classifier Example

To perform a basic comparison between a CDNN and QDNN classifier, we generate data from two classes and then attempt to separate them. Classification data comes in pairs $\{X, y\}$, where X is a vector of n input features and y is the target value 0 or 1. The CDNN used has an architecture of n inputs, a layer of 8 hidden perceptrons, and an output perceptron. A binary cross entropy loss function and the Adam optimization algorithm are used.

When classifying, 100 epochs are used for training the CDNN.

In QNNs, the number of nodes in hidden layers is often structured as $\log_2(N)$, where N is the number of input variables. This design leverages the principles of quantum computational efficiency and the information-encoding properties of quantum systems. In quantum computing, a system of n qubits can represent 2^n states simultaneously through quantum superposition and entanglement [31]. To efficiently process N classical input variables, encoding them into $\log_2(N)$ qubits provides a compact representation, minimizing redundancy in quantum resources [21].

Because the quantum circuits rely on unitary transformations, and well-designed QNNs aim to minimize circuit depth to reduce computational complexity and mitigate errors in noisy quantum hardware [32]. Structuring hidden layers with $\log_2(N)$ nodes helps maintain an optimal balance between circuit depth and width, facilitating efficient parameterization of quantum gates. This logarithmic scaling aligns with several quantum algorithms, such as the Quantum Fourier Transform (QFT) and variational quantum circuits, which often employ log-scaled structures to achieve logarithmic or near-logarithmic circuit depth [33, 34].

A key reason for the logarithmic scaling of nodes in QNNs is the role of quantum entanglement in modeling feature correlations. Entanglement enables QNNs to efficiently capture dependencies between input variables, allowing a logarithmic number of qubits to encode and manipulate these relationships effectively [35]. Using more nodes than necessary introduces redundant parameterization, which can increase computational overhead and risk overfitting, while too few nodes may restrict the network's capacity to learn complex correlations [21]. Furthermore, QNNs offer potential advantages in data compression and computational speedup compared to classical deep learning architectures. CDNNs often require deep architectures with many layers to capture intricate patterns, whereas QNNs, leveraging the high-dimensional Hilbert space, can represent complex functions with significantly fewer parameters [36]. A logarithmic scaling of hidden nodes balances the trade-off between expressive power and computational efficiency, ensuring feasible quantum learning implementations.

In QML, feature encoding into a Hilbert space typically involves unitary transformations applied to a quantum state defined by $\lceil \log_2 N \rceil$ qubits, where N is the dimension of the input feature space. This logarithmic scaling ensures efficient representation of classical data in a quantum system. Quantum variational classifiers, a common QML architecture, utilize this approach to map input features into a quantum state, optimizing circuit depth and leveraging quantum entanglement for potential computational advantages, such as quantum speedup in specific tasks [37]. The use of $\lceil \log_2 N \rceil$ qubits in encoding and subsequent layers reflects a design choice that aligns with the principles of quantum computation, bal-

TABLE I: Comparison of CDNN and QDNN classification efficiency for different data sets. Our default data set is 3 function data with 250 training pairs, 8 input features, and 0.05 noise; each row varies one of these factors while holding the rest at the default. The QDNN classification efficiency is higher than the CDNN classification efficiency for all datasets classified, indicating universal QDNN outperformance in this classification task. Fewer training pairs, higher data complexity, more input features, and lower noise lead to greater QDNN outperformance.

Factor varied	Change	CDNN eff.	QDNN eff.	QDNN/CDNN ratio change
Number of training pairs	500 pairs \rightarrow 50 pairs	0.6436 \rightarrow 0.4716	0.8745 \rightarrow 0.8116	27%
Data complexity	1 function data \rightarrow 3 function data	0.8378 \rightarrow 0.6290	0.9678 \rightarrow 0.8704	20%
Number of input features	8 features \rightarrow 16 features	0.6290 \rightarrow 0.5327	0.8704 \rightarrow 0.9359	27%
Noise	$0.2\sigma \rightarrow 0.05\sigma$	0.7917 \rightarrow 0.8378	0.8704 \rightarrow 0.9678	5%

ancing expressivity and computational efficiency in quantum neural networks [21].

The classification pair $\{X, y\}$ is converted into the form $\{|\phi^{\text{in}}\rangle, |\phi^{\text{target}}\rangle\}$ for the QDNN. This is done by converting an N -dimensional input vector X into a $\lceil \log_2 N \rceil$ -qubit state. Specifically, some input vector

$$X = \begin{pmatrix} x_1 \\ x_2 \\ \vdots \\ x_N \end{pmatrix}, \quad (35)$$

is converted into an N -dimensional quantum state $|\phi^{\text{in}}\rangle$ of the form

$$|\phi^{\text{in}}\rangle = \frac{x_1|00\dots 0\rangle + x_2|00\dots 1\rangle + \dots + x_N|11\dots 1\rangle}{\sqrt{x_1^2 + x_2^2 + \dots + x_N^2}}. \quad (36)$$

The target value $y = 0$ is converted to the target state $|\phi^{\text{target}}\rangle = |0\rangle$, and the target value $y = 1$ is converted to the target value $|\phi^{\text{target}}\rangle = |1\rangle$. To mirror the CDNN architecture, the QDNN architecture is set to $\lceil \log_2 N \rceil$ input qubits, a layer of 3 hidden quantum perceptrons, and an output quantum perceptron. When classifying, 25 epochs are used for training the QDNN.

To vary data complexity, we generate two types of classification data: 1 function data, in which the two classes of data are produced using only a single function, and 3 function data, in which the two classes of data are produced using three functions. 1 function signal data ($y = 1$) is first generated by sampling each input feature x_i from a normal distribution with a mean of 1.0 and a standard deviation of 0.5:

$$x_i \sim \mathcal{N}(1.0, 0.5^2). \quad (37)$$

Then, to introduce correlations, each feature x_i is updated based on the other features x_j (with $i \neq j$) using the transformation:

$$x_i \leftarrow x_i + 0.1 \sin(\pi x_j) + \epsilon, \quad (38)$$

where $\epsilon \sim \mathcal{N}(0.0, \sigma^2)$ and σ is a noise parameter. Similarly, 1 function background data ($y = 0$) is generated with a normal distribution

$$x_i \sim \mathcal{N}(0.0, 1.0^2), \quad (39)$$

then is transformed using

$$x_i \leftarrow x_i + 0.1 \cos(\pi x_j) + \epsilon. \quad (40)$$

3 function signal data and background data are also initially drawn from Eqs. (37) and (39), respectively, but undergo three complex transformations instead of one. Specifically, signal data is transformed with

$$\begin{aligned} x_i &\leftarrow x_i + 0.1 \sin^2(\pi x_j) + \epsilon_1 \\ x_i &\leftarrow x_i + 0.1 \log^2(|x_j| + 1) + \epsilon_2 \\ x_i &\leftarrow x_i + 0.1 e^{-|x_j|} + \epsilon_3, \end{aligned} \quad (41)$$

and background data is transformed with

$$\begin{aligned} x_i &\leftarrow x_i + 0.1 \cos^2(\pi x_j) + \epsilon_1 \\ x_i &\leftarrow x_i + 0.1 \tan^2(x_j) + \epsilon_2 \\ x_i &\leftarrow x_i + 0.1 e^{-|x_j|} + \epsilon_3, \end{aligned} \quad (42)$$

where $\epsilon_1, \epsilon_2, \epsilon_3 \sim \mathcal{N}(0.0, \sigma^2)$.

In Table I, we summarize how our CDNN and QDNN models respond to changes in the number of training pairs, the complexity of the data, the number of input variables, and the noise level. Each of these factors is varied individually, with the other three held constant. We use classification efficiency as the metric to measure the quality of the classifications. Considering output values of 1 to be “positive” and output values of 0 to be “negative,” it is defined to be the average of the true positive (TP) rate, true negative (TN) rate, and accuracy. When comparing the QDNN classification efficiencies with those of the CDNN for any of the datasets, it is clear that the QDNN outperforms the CDNN in the classification of this complex data. The table also indicates that while noise plays a role in QDNN outperformance, the most important factors for QDNN outperformance are the number of training pairs, data complexity, and the number of input variables. Specifically, the QDNN outperformance is higher when the number of training pairs is decreased from 500 to 50, the data complexity is increased from 1 function data to 3 function data, and the number of input variables is increased from 8 features to 16 features.

However, although QDNN outperformance is optimized for complex datasets, the classification comparison

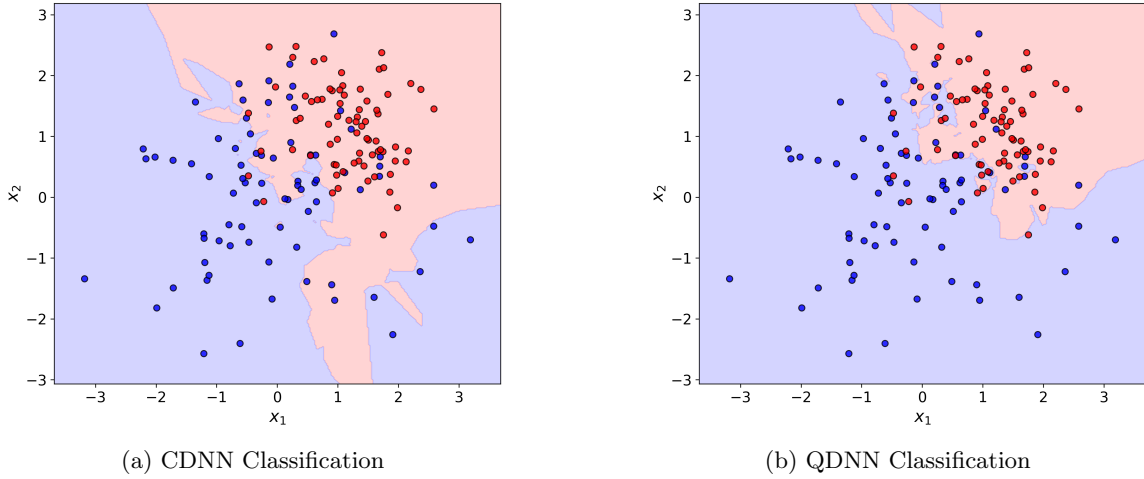


FIG. 3: Classification comparison of 1 function data, generated by Eqs. (37)-(40) with 0.2σ noise level, and 8 input features. Two of the eight input features are plotted, with signal points in red and background points in blue. The QDNN outperforms the CDNN in classification accuracy.

presented in Fig. 3 demonstrates a notable performance advantage of the QDNN over the CDNN even for a relatively simple dataset (for visual clarity) with 1 function data, 8 input features, and 0.2σ noise level. The visualization of two selected input features highlights the QDNN's ability to distinguish signal (red) from background (blue) points. Specifically, the confusion matrix [38] for the CDNN (\mathbf{C}^{CDNN}) and QDNN (\mathbf{C}^{QDNN}) are

$$\mathbf{C}^{\text{CDNN}} = \begin{bmatrix} 70 & 24 \\ 4 & 52 \end{bmatrix}, \quad \mathbf{C}^{\text{QDNN}} = \begin{bmatrix} 65 & 6 \\ 9 & 70 \end{bmatrix}, \quad (43)$$

where $C_{11} = \text{TP}$, $C_{12} = \text{FP}$ (false positive rate), $C_{21} = \text{FN}$ (false negative rate), and $C_{22} = \text{TN}$. This equates to a 0.8144 classification efficiency for the CDNN compared to a 0.8998 classification efficiency for the QDNN.

Our classifier results suggest a notable advantage in using a QDNN for classification, consistent with previous investigations [39–43]. However, further investigation is warranted to assess the generalizability of this advantage across diverse datasets and to address potential challenges, such as noise sensitivity and computational overhead, which could impact practical deployment.

B. Quantum Regression

QDNNs for regression differ from CDNNs in their approach to modeling continuous outputs, leveraging quantum properties to enhance efficiency in specific scenarios. Unlike CDNNs, which rely on layered architectures with polynomial parameter scaling to fit regression functions, QDNNs encode input data into quantum states within a 2^n -dimensional Hilbert space for n qubits, similar to what was previously described for classification. Theoretically, QDNNs can achieve more compact representations of

complex, high-dimensional functions with fewer parameters than CDNNs, particularly for regression tasks involving quantum-native functions, such as those in particle and nuclear physics [29]. For regression tasks, QDNNs use variational quantum circuits (VQCs) to optimize continuous loss functions, such as mean squared error, by adjusting quantum gate parameters via the parameter-shift rule [20]. This allows QDNNs to efficiently capture non-linear relationships in data, particularly for tasks where high-dimensional correlations are prevalent.

A key distinction in regression is the QDNN's ability to exploit entanglement to model intricate dependencies in continuous data, potentially reducing the training complexity compared to CDNNs, which may require exponentially more parameters to achieve similar accuracy for certain function classes [25]. However, QDNN regression, similar to QDNN classification, faces unique challenges related to barren plateaus that require careful circuit design with controlled entanglement to maintain trainability [28]. While CDNNs are robust for general regression, their performance can degrade in high-dimensional settings due to vanishing gradients [26], whereas QDNNs show promise for specialized regression tasks with structured data.

1. Quantum Regression Example

As a preliminary comparison, we performed some basic regression tests on a CDNN and QDNN. To do this, we generate data sets by plugging 100 evenly distributed values $x_i \in [-2, 4]$ into six target functions with varying complexity: Eqs. (A1)-(A6), listed in the Appendix. Then, we introduce some noise in the data with the transformation,

$$y_i \leftarrow y_i + \mathcal{N}(0.0, \sigma^2), \quad (44)$$

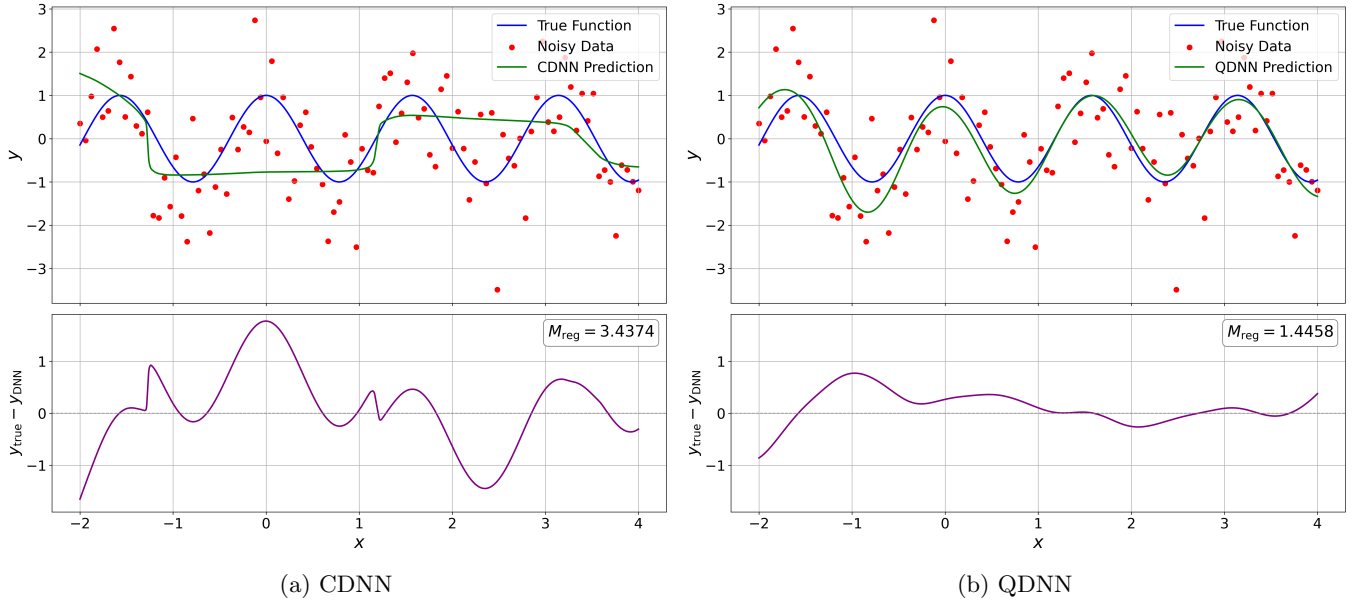
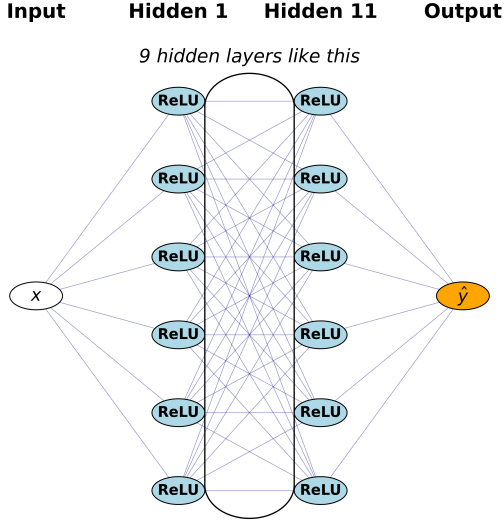


FIG. 4: A function regression comparison between a) CDNN and b) QDNN using target Function Eq. (A1), with 1σ noise level, and trained using 50 epochs. A difference plot between the true function and DNN prediction is shown, and the integral of the absolute value of the difference curve M_{reg} [Eq. (45)] is reported indicating a smaller deviation from the QDNN than the CDNN. The QDNN outperforms with $\Xi = 1.378 > 0$.



Simplification: Each hidden node represents ~ 10 neurons of the full 64 per layer

FIG. 5: A schematic representation of a CDNN architecture for regression. The network takes a scalar input and passes it through a sequence of fully connected hidden layers with 64 neurons each, using ReLU activations. For clarity, only the first and last hidden layers are shown explicitly; the 9 intermediate layers are represented by a bracketed simplification. The final output layer produces a single continuous value, suitable for the regression.

where the standard deviation σ takes the values $\sigma = 0.1, 0.25, 1.0$ for each of the six target functions. This gives us 15 sets of 100 noisy data points (x_i, y_i) on which we perform a regression with the CDNN and QDNN.

To judge the quality of a given DNN fit, we use a simple regression metric M_{reg} defined by

$$M_{\text{reg}} = \int_{x_{\min}}^{x_{\max}} |y_{\text{DNN}}(x) - y_{\text{true}}(x)| dx. \quad (45)$$

Here, a value of $M_{\text{reg}} = 0$ indicates a perfect fit. An example regression is shown in Fig. 4, where we present the CDNN and QDNN regression on a set of noisy data generated from Function Eq. (A1): $y = \cos 4x$.

Some values of M_{reg} for both the CDNN and QDNN are displayed in Tables VI-XI in the Appendix. Using these metric values, we calculate the quantum outperformance Ξ for a given data set and number of epochs by

$$\Xi = M_{\text{reg}}^{\text{CDNN}} / M_{\text{reg}}^{\text{QDNN}} - 1. \quad (46)$$

Therefore, $\Xi > 0$ indicates that the QDNN outperforms, and $\Xi < 0$ indicates the CDNN outperforms. The magnitude of Ξ indicates the extent to which the better DNN outperforms.

An example regression is shown in the top portion of Fig. 4b comparing a) CDNN and b) QDNN using target Function Eq. (A1), with 1σ noise level, and trained using 50 epochs. A difference plot between the true function and DNN prediction is shown in the lower portion, and the integral of the absolute value of the difference

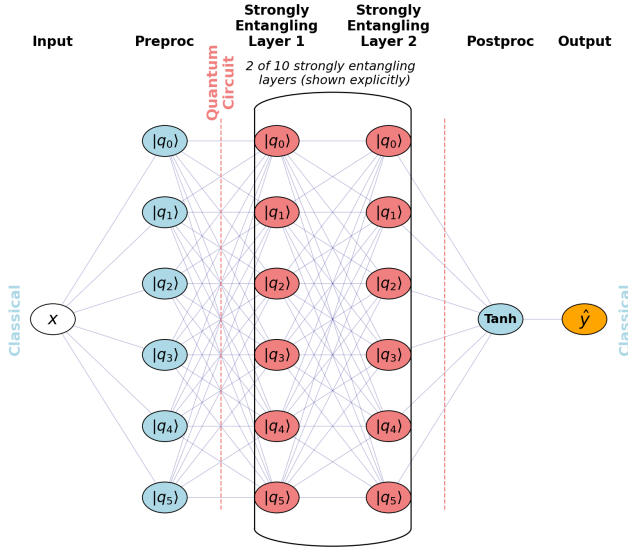


FIG. 6: A schematic representation of a QDNN architecture for regression. The model begins with a classical preprocessing layer that maps input data to 6 qubits. These values are embedded into quantum states using angle embedding and passed through 10 layers of Strongly Entangling Layers acting on 6 qubits. Three of these layers are shown explicitly for clarity. After the final entangling layer, Pauli-Z expectation values $\langle Z \rangle$ are measured on each qubit, yielding classical outputs.

These outputs are processed through a classical postprocessing network, consisting of a hidden layer with 64 neurons and a Tanh activation, followed by a linear output neuron.

curve M_{reg} [Eq. (45)] is reported clearly demonstrating a smaller deviation from the QDNN than the CDNN. The QDNN outperforms with $\Xi = 1.378 > 0$.

2. Quantum Qualifier

Identifying in advance whether a particular function type or dataset is more amenable to parameter extraction using a QDNN or a CDNN can provide a significant methodological advantage. Establishing such a diagnostic metric enables preliminary analysis to determine whether a QDNN can offer a quantifiable reduction in error or improved robustness. To systematically evaluate and quantify this potential advantage, a range of complexity and information-theoretic metrics can be employed to construct a composite *quantum qualifier*. Among the most informative of these are the nonlinearity measure (\mathfrak{N}), frequency complexity (Φ), fractal dimension (\mathfrak{D}), mutual information (\mathfrak{M}), and Fourier transform complexity (\mathfrak{F}). These metrics provide complementary insights into the structural and informational properties of the target function or dataset, helping to guide the choice between QDNN and CDNN architectures.

Nonlinearity [44] (\mathfrak{N}) measures the deviation of a dataset (x_i, y_i) from a linear trend and can reveal the expressive power of a model in capturing nonlinear relationships. To compute it, we first perform a linear regression on the set of data points (x_i, y_i) , which yields points $(x_i, \hat{y}_i^{\text{lin}})$. Then, the nonlinearity metric is defined to be the ratio between the residual sum of squares of the linear fit and the residual sum of squares from the mean:

$$\mathfrak{N} = \frac{\sum_{i=1}^n (y_i - \hat{y}_i^{\text{lin}})^2}{\sum_{i=1}^n (y_i - \bar{y})^2}, \quad (47)$$

where

$$\bar{y} = \frac{1}{n} \sum_{i=1}^n y_i. \quad (48)$$

Values of \mathfrak{N} near 0 indicate the data is well-approximated by a linear model, while values closer to 1 suggest higher nonlinearity. In the quantum setting, parameterized quantum circuits have been shown to exhibit enhanced nonlinear representational capacity. Du *et al.* [29] demonstrate that QDNNs possess a richer functional landscape than classical models due to quantum operations that naturally induce nonlinearity. This implies that datasets exhibiting high nonlinearity may be more efficiently modeled by QDNNs, making the nonlinearity metric a useful indicator of potential quantum advantage.

Frequency complexity (Φ), which counts the number of local maxima in a signal's power spectrum, provides insight into the oscillatory structure and richness of data representations [45]. To compute it, we first perform a discrete Fourier transform on the set of y values: $y \xrightarrow{\mathcal{F}} \hat{y}$. Letting \hat{y}_k denote the k th Fourier coefficient, we compute the dataset's power spectrum: $P_k = |\hat{y}_k|^2$, which represents the contribution of each frequency component. The frequency complexity is defined as the number of local maxima (peaks) in the power spectrum:

$$\Phi = |\{k \mid P_k \text{ is a local maximum}\}|. \quad (49)$$

A higher value indicates that the dataset contains a greater number of distinct frequency components, reflecting increased structural or oscillatory complexity. The Quantum Fourier Convolutional Neural Network proposed by Shen and Liu shows that QDNNs leveraging quantum Fourier transforms can outperform classical CNNs in frequency-domain processing [46]. The exponential speed-up in extracting and interpreting frequency components underscores the utility of frequency complexity as a tool for identifying cases where QDNNs may offer significant advantages.

Fractal dimension [47] (\mathfrak{D}) quantifies the detailed complexity or roughness of the dataset. While the fractal dimension is less commonly applied in direct QDNN benchmarking, it serves as a proxy for structural complexity. Here, we compute the box-counting dimension of the data points. We first choose a logarithmically spaced series of box sizes s_k from 1 to N , the number of data points.

Then, for each box size s_k , we partition the set of y values into non-overlapping segments of size s_k and take a

normalized sum over the range of the y values within each segment:

$$C(s_k) = \frac{1}{s_k} \sum_{i=0}^{\lfloor N/s_k \rfloor - 1} (\max(y_{is_k}, y_{is_k+1}, \dots, y_{(i+1)s_k-1}) - \min(y_{is_k}, y_{is_k+1}, \dots, y_{(i+1)s_k-1})). \quad (50)$$

Finally, we perform a linear regression on $\log C(s_k)$ against $\log s_k$, yielding

$$\log C(s_k) = -\mathfrak{D} \log s_k + \text{const.} \quad (51)$$

The negative slope \mathfrak{D} is the fractal dimension, where a higher value of \mathfrak{D} indicates a more complex or rough structure. Verdon *et al.* [48] discuss how quantum neural architectures can more efficiently model highly structured sequences that exhibit self-similar or hierarchical properties—traits often captured by high fractal dimension. Thus, this metric can be applied to characterize tasks where QDNNs offer improved performance through their natural alignment with high-dimensional, complex data manifolds.

Mutual information [49] (\mathfrak{M}) quantifies the amount of information shared between input and output variables and is an established metric for evaluating the information retention capacity of neural networks. In general, the mutual information between two variables X and Y is defined as:

$$I(X; Y) = H(X) + H(Y) - H(X, Y), \quad (52)$$

where $H(X)$ and $H(Y)$ are the entropies of X and Y , respectively, and $H(X, Y)$ is the joint entropy of X and Y . The entropy of a variable is a measure of uncertainty, while the joint entropy captures the uncertainty in the combined system of X and Y . Here, mutual information is computed using a contingency table, which represents the joint probability distribution of the two variables. For our given set of data points (x_i, y_i) , we first compute their 2D histogram, which gives the joint distribution of x and y . The mutual information is then calculated by summing over all possible pairs of values (x_i, y_j) in the contingency table as follows:

$$\mathfrak{M} = \sum_{i,j} \frac{n_{ij}}{N} \log \left(\frac{n_{ij}/N}{(\sum_i n_{ij}/N)(\sum_j n_{ij}/N)} \right), \quad (53)$$

where n_{ij} represents the count in the (i, j) -th cell of the 2D histogram, and N is the total number of data points. This formula evaluates how much knowing one variable reduces the uncertainty about the other by considering their joint distribution and the marginal distributions of each variable. Basilewitsch *et al.* [50] conduct a comparative study of QDNNs and CDNNs, showing that quantum models often preserve and utilize mutual information

more effectively due to entanglement and superposition. Therefore, mutual information serves not only as a metric of model performance but also as a diagnostic tool for identifying scenarios in which quantum information processing offers clear benefits.

Lastly, Fourier transform complexity [51] (\mathfrak{F}), defined as the total energy contained in the frequency domain, reflects the signal richness and processing capacity of a model and is computed through a process similar to the frequency complexity (Φ). Specifically, we perform a discrete Fourier transform on the set of y values and compute the power spectrum: $P_k = |\hat{y}_k|^2$. The Fourier transform complexity is defined as the sum of the power spectrum:

$$\mathfrak{F} = \sum_k P_k. \quad (54)$$

A higher \mathfrak{F} indicates that the data has a greater amount of variability as it progresses in the domain. In the context of high-energy physics, Chen *et al.* [52] demonstrate that Quantum Convolutional Neural Networks (QCNNs) trained on event classification tasks outperform classical CNNs by leveraging their superior frequency-domain analysis capabilities. This validates the Fourier complexity metric as a relevant benchmark for comparing quantum and classical architectures, particularly for tasks with substantial spectral content.

Together, these metrics offer a multidimensional framework for understanding when and why QDNNs may outperform classical models. They provide a principled way to diagnose task complexity, model capacity, and potential quantum advantage. These metrics can be used to construct a composite quantum qualifier $\hat{\Xi}$ that can be used to estimate quantum outperformance Ξ based purely on characteristics of the data. Specifically, we examined the five different function characteristics, namely, nonlinearity (\mathfrak{N}), frequency complexity (Φ), fractal dimension (\mathfrak{D}), mutual information (\mathfrak{M}), and Fourier transform complexity (\mathfrak{F}), for correlations with quantum outperformance Ξ .

In Tables XII, XIII, and XIV in the Appendix, we show the values of these five function characteristics for each of the target functions with 0.1σ , 0.25σ , 1σ noise level, respectively. We then use Eq. (46) to calculate the quantum outperformance Ξ for each of the tests, and we analyze the values of Ξ for a given number of epochs against each of the five function characteristics. We perform linear regressions on this and display the results in

TABLE II: Summary of the DVCS data from JLAB used in this analysis. The table includes information on the data source and the kinematic range covered by the helicity-independent cross section.

Experiment	Publication Year	E_{beam} (GeV)	Q^2 (GeV ²)	$-t$ (GeV ²)	x_B	Number of Points
Hall A E12-06-114 [53]	2022	4.487 - 10.992	2.71 - 8.51	0.204 - 1.373	0.363 - 0.617	1080
Hall A E07-007 [54]	2017	3.355 - 5.55	1.49 - 2.	0.177 - 0.363	0.356 - 0.361	404
Hall A E00-110 [55]	2015	5.75	1.82 - 2.37	0.171 - 0.372	0.336 - 0.401	468
Hall B e1-DVCS1 [56]	2015	5.75	1.11 - 3.77	0.11 - 0.45	0.126 - 0.475	1933

Tables XV and XVI, which indicate the correlation between quantum outperformance and the characteristics of the target function data for a given number of epochs. Using this information, we fit polynomial curves (and an exponential curve for \mathfrak{N}) to the regression slopes and R^2 values as a function of the number of epochs. Since the polynomial fit of the regression slopes against the number of epochs approximates the correlation between quantum outperformance Ξ and a given function characteristic, we construct a linear function corresponding to this correlation for a given number of epochs. Finally, we define the quantum qualifier $\hat{\Xi}$ by summing all of these linear functions (with slope given by the Ξ regression slope polynomial fit) and then weighting by the strength of the correlation (given by the R^2 polynomial fit):

$$\hat{\Xi} = e^{-\alpha n} \sum_{i=0}^2 \beta_{1i} n^i X_1 + \sum_{j=2}^5 \sum_{i=0}^4 \beta_{ji} n^i X_j. \quad (55)$$

This quantum qualifier can estimate the value of Ξ based on the five function characteristics and the number of epochs n that the CDNN and QDNN are trained on. Here, the coefficients are parameterized in one indexed set β_{ji} , where j indexes the corresponding observable X_j :

$$X_j \in \{\mathfrak{N}-0.25, \Phi-24.5, \mathfrak{D}-0.95, \mathfrak{M}+0.05, \mathfrak{F}-4999.5\}. \quad (56)$$

The exponential prefactor $e^{-\alpha n}$ is included explicitly (with $\alpha = 0.0101$), and parameters β_{ji} encode all coefficients. α is a fixed scalar in the exponential. The outer sum j runs over different offset parameters ($\mathfrak{N}, \Phi, \mathfrak{D}, \mathfrak{M}, \mathfrak{F}$), each scaled by a specific offset. The inner sum \sum_i runs over powers of n , representing polynomial dependence. Table XVII in the Appendix shows the numerical parameters of the quantum qualifier expression.

Equation (55) captures the main conclusions that are immediately evident from Tables XV and XVI; for example, that mutual information \mathfrak{M} has the most positive correlation with quantum outperformance, while fractal dimension \mathfrak{D} has the most negative and strongest correlation with quantum outperformance. We will return to the idea of a quantum qualifier in Sec. VI, where we construct a simpler version specifically for the DVCS process, which we will use to help determine if a QDNN is advantageous in CFF extraction. For now, having thoroughly discussed the structure and application of QDNNs, we will detail the preparation of the data essential for training and validating these models in the context of CFF

extraction. It is worth noting that this process of testing data and constructing a quantum qualifier can be done for any formalism, at any twist approximation, or for any set of observables, with sensitivity to error and data sparsity. The construction of such metrics may have great utility for other hadronic physics applications.

IV. EXPERIMENTAL DATA AND PSEUDODATA GENERATION

The CFF extraction analyses detailed in the remainder of this paper utilize DVCS experimental data from Hall A [53–55] and Hall B [56] at Jefferson Lab (JLab). The dataset, summarized in Table II, includes both helicity-independent and helicity-dependent cross sections. However, our focus is exclusively on the helicity-independent (unpolarized) cross sections for simplicity. The data is finely binned in a fourfold differential cross section parameterized by Q^2 , x_B , t , and ϕ , comprising a total of 3,885 data points for analysis.

The dataset spans measurements from both the 6 GeV and 12 GeV JLab experimental programs. The 12 GeV data extend to higher values of Q^2 , reaching up to 8.4 GeV², while the 6 GeV-era data cover lower ranges. The majority of the data points originate from the e1-DVCS1 experiment at Hall B [56], which operated with a fixed beam energy of 5.75 GeV and probed a Q^2 range from 1.0 to 4.6 GeV². These experimental data sets serve as a crucial foundation, not only for generating realistic pseudodata, but also to establish initial benchmarks for developing and validating our machine learning techniques, enabling systematic comparisons between CDNNs and QDNNs under controlled conditions.

A. Pseudodata Generation

We now generate numerous pseudodata sets based directly on the experimental data sets. These pseudodata sets allow us to precisely control the “true” CFF values, offering a controlled environment for testing and evaluating the accuracy and performance of our neural network models before their application to real experimental data, where the true values are unknown. Our pseudodata sets are generated using the following *basic* model function:

$$G(x_B, t) = (ax_B^2 + bx_B)e^{ct^2+dt+e} + f, \quad (57)$$

TABLE III: The parameters used in Eq. (57) to generate the pseudodata set.

CFFs	a	b	c	d	e	f
$\Re\mathcal{H}$	-4.41	1.68	-9.14	-3.57	1.54	-1.37
$\Re\mathcal{E}$	144.56	149.99	0.32	-1.09	-148.49	-0.31
$\Re\tilde{\mathcal{H}}$	-1.86	1.50	-0.29	-1.33	0.46	-0.98
$DVCS$	0.50	-0.41	0.05	-0.25	0.55	0.166

where $G(x_B, t)$ represents the CFFs and DVCS cross section components: $\Re\mathcal{H}$, $\Re\mathcal{E}$, $\Re\tilde{\mathcal{H}}$, and $DVCS$. The parameters $\{a, b, c, d, e, f\}$ for each case are listed in Table III, and are based on initial tests. The structure of this model function allows for linear or non-linear changes in x_B with exponential flexibility in t . The parameterization has no physical meaning as the model is purely designed for testing the DNN extractions.

To compute the photon leptoproduction cross section described in Section II, the CFFs are taken from the *basic* model. Within each kinematic bin, the cross section is randomly sampled from a Gaussian distribution centered on the calculated value at each ϕ point, with the standard deviation corresponding to experimental uncertainties. The generated kinematic settings and ϕ points match those of the experimental data used in this study, ensuring that acceptance effects and statistical limitations are properly accounted for.

The uncertainties introduced in the pseudodata are taken from the reported experimental errors from JLab data [53–56], which include both statistical and systematic contributions. As a result, the generated pseudodata closely replicate real-world experimental conditions that influence the measured cross sections.

To account for statistical fluctuations in the data analysis, a set of replica datasets is produced for each pseudodata configuration. In each replica, the cross section at the central value of each bin is resampled using Gaussian noise consistent with the original experimental uncertainty. This ensemble approach enables a robust estimation of the variability in extracted observables due to measurement uncertainty.

With this ensemble of realistic pseudodata in hand, we proceed to the central task of our study: extracting CFFs using both classical and quantum deep neural networks, and directly comparing their respective performance across the full range of kinematics.

V. PSEUDODATA CFF EXTRACTION

In this section, we focus exclusively on local fitting and compare our two deep neural network approaches—CDNNs and QDNNs—for extracting CFFs from the pseudodata.

Traditional local fits extract CFFs independently at each kinematic point, typically using data binned in the

azimuthal angle ϕ , which describes the relative orientation of the lepton and hadron scattering planes. The fitting procedure is based on the helicity amplitudes and is performed separately for each kinematic bin. While this method avoids assumptions about underlying functional forms, it can lead to non-uniqueness in extracted CFFs due to limited constraints, often resulting in large systematic uncertainties. DNN-based fitting methods offer an alternative approach by using statistical correlations across the dataset to improve extraction precision. Unlike analytical parameterizations that impose model-specific constraints, these neural network methods learn directly from experimental data without requiring predefined functional dependencies or initial guesses of the CFFs.

We compare the performance of CDNNs and QDNNs in extracting CFFs, assessing their effectiveness through a testing phase using pseudodata generated at the same kinematics as the experimental data. The main evaluation metrics we use are accuracy and precision. Accuracy $\epsilon(k, Q^2, x_B, t)$ quantifies how closely the mean of the DNN-extracted CFFs aligns with the true CFF values used in pseudodata generation:

$$\epsilon(k, Q^2, x_B, t) = |CFF_{\text{DNN}} - CFF_{\text{true}}|. \quad (58)$$

This metric is actually the absolute value of the residual used to define accuracy, which remains meaningful even if CFF_{DNN} and CFF_{true} are not less than 1. The precision $\sigma(k, Q^2, x_B, t)$ reflects the variation in extracted CFFs across multiple replicas:

$$\sigma(k, Q^2, x_B, t) = \sqrt{\frac{\sum_i (CFF_{\text{DNN}}^i - \overline{CFF_{\text{DNN}}})^2}{N}}. \quad (59)$$

The generating function used to produce the *true* CFF values follows a *basic* model from Eq. (57) using parameters from Table III, and the pseudodata we extract the CFFs from is described in Sec. IV A.

In this section, we aim to compare CDNN and QDNN approaches, evaluating their ability to extract CFFs with improved accuracy, precision, and reliability. We consider two QDNN models: the Basic QDNN described in the next section (Sec. V A) and the Full QDNN described in following section (Sec. V B). The Basic QDNN is designed to mirror the CDNN model in architecture and complexity, serving as a baseline comparison without quantum-specific optimization. The Full QDNN is designed to fully take advantage of the quantum potential by carefully mitigating quantum-specific challenges and incorporating quantum-specific optimization schemes. The details of the architecture and construction of the CDNN and QDNNs, the method of extraction, and the corresponding results are presented in the following subsections.

A. Basic QDNN

We begin by performing the CFF extraction using a CDNN model and a Basic QDNN model (which we refer to as just QDNN in this section). This extraction serves to gauge the immediate advantages and disadvantages of a direct transition to a quantum-based model before considering quantum-specific effects.

All the DNN models used for extraction in this paper have a three-dimensional input (x_B, Q^2, t) , the kinematic values of a given kinematic bin, and a four-dimensional output $(\text{Re}\mathcal{H}, \text{Re}\mathcal{E}, \text{Re}\tilde{\mathcal{H}}, \text{DVCS})$, the four CFFs. The DNNs use a custom, physics-informed loss function that predicts the cross section F using the outputted three CFFs and DVCS term with the BKM10 formalism (Sec. II) and computes the mean squared error of the predicted cross section against the true cross section. The specific model architectures of the CDNN and QDNN are described as follows.

The CDNN model used for CFF extraction is based closely on the regression CDNN model described in Sec. IIIB and shown in Fig. 5. The input layer of the CDNN maps the three-dimensional input layer (x_B, Q^2, t) to 64 neurons. Then, there are 8 hidden layers, each with 64 neurons and ReLU activation. Finally, the output layer maps the 64 features to a four-dimensional output $(\text{Re}\mathcal{H}, \text{Re}\mathcal{E}, \text{Re}\tilde{\mathcal{H}}, \text{DVCS})$. The QDNN is constructed based on the architecture of the CDNN and is similar to the architecture shown in Fig. 6. The input layer of the QDNN is a classical linear preprocessing layer, mapping the three-dimensional input to 6 qubits, which is equivalent to the 64 neurons used in the CDNN (Sec. III). The input data is then embedded into quantum state space using angle embedding, which encodes the features as rotation angles on the qubits. Next, there are 8 hidden Strongly Entangling Layers, consisting of rotations and entanglers. Finally, the expectation value of the Pauli-Z operator for each qubit is measured. In the classical postprocessing layers, the 6 quantum outputs are mapped to 64 neurons, followed by a Tanh activation, then another linear layer to the final four-dimensional output.

In the remainder of this section, we first perform a thorough analysis of the model complexities of the CDNN and QDNN in order to show quantitatively that the two models are similar in complexity (Sec. VA1). Then, we use the models to extract the CFFs from the pseudodata and perform a detailed error analysis (Sec. VA2).

1. Model Complexity

To compare the CDNN and QDNN fairly, we must ensure that neither model has an inherent advantage simply due to size or computational power. Therefore, in this section, we compute values of several quantitative metrics that aim to characterize and compare the complexity of the CDNN and QDNN architectures employed for the extraction of CFFs from noisy pseudodata. Specifically,

we focus on the number of trainable parameters and the estimated number of floating point operations per second (FLOPs), which serve as metrics for a model's capacity and computational cost, respectively. The goal of this analysis is to demonstrate that the CDNN and Basic QDNN are comparable in the sense that they operating at roughly the same level of complexity in terms of the size and depth of the model, even though they come from very different paradigms.

However, even though we model the architecture of the Basic QDNN on that of the CDNN, making such a head-to-head comparison is not so straightforward because CDNNs and QDNNs are fundamentally different. For example, in a QDNN, the number of trainable parameters (e.g., rotation angles) may be relatively small, but the entangled structure of quantum circuits can, in principle, encode highly non-linear transformations that would require a much larger classical network to approximate. Similarly, estimating FLOPs in quantum circuits is nontrivial because quantum gates do not execute classical floating point operations, and instead evolve qubit states via unitary transformations, which scale differently depending on circuit depth and entanglement structure. Still, calculating these architectural metrics is a valuable starting point. They give us a baseline for comparing the CDNN and QDNN models side by side and ensure that we are not giving one model an unfair advantage simply by making it larger or more powerful.

For a fully connected layer with input size M and output size N , the number of trainable parameters P is

$$P = MN + N \quad (\text{weights} + \text{biases}). \quad (60)$$

For the CDNN, we have trainable parameters in the input layer ($3 \rightarrow 64$), 8 hidden layers ($64 \rightarrow 64$), and output layers ($64 \rightarrow 4$). Therefore, the total number of trainable parameters in the CDNN is

$$\begin{aligned} P_{\text{CDNN}} &= P_{\text{in}} + 8P_{\text{hid}} + P_{\text{out}} \\ &= (3 \cdot 64 + 64) + 8(64 \cdot 64 + 64) + (64 \cdot 4 + 4) \\ &= 33796. \end{aligned} \quad (61)$$

For the QDNN, we have trainable parameters in the preprocessing layer ($3 \rightarrow 6$), 8 Strongly Entangling Layers ($6 \rightarrow 6$), and the postprocessing layers ($6 \rightarrow 64 \rightarrow 4$). The angle embedding layer is a fixed operation that contains no trainable parameters. In the Strongly Entangling Layers, each qubit undergoes three parameterized rotations, and since there are 8 Strongly Entangling Layers and 6 qubits per layer,

$$P_{\text{SEL}} = 8 \cdot 6 \cdot 3 = 144. \quad (62)$$

Therefore,

$$\begin{aligned} P_{\text{QDNN}} &= P_{\text{pre}} + P_{\text{SEL}} + P_{\text{post}} \\ &= (3 \cdot 6 + 6) + 144 + ((6 \cdot 64 + 64) + (64 \cdot 4 + 4)) \\ &= 876. \end{aligned} \quad (63)$$

TABLE IV: Comparison of model complexity between the CDNN and the QDNN. The table lists key architectural metrics, including depth (layer composition), width (neurons or qubits), number of trainable parameters, and estimated floating-point operations (FLOPs). The QDNN includes both quantum and classical layers, with a 64-dimensional quantum encoding based on 6 qubits.

Metric	CDNN	QDNN
Depth	10 layers (2 in/out + 8 hidden)	11 layers (8 quantum + 3 classical)
Width	64 neurons	6 qubits (64-dimensional)
Trainable Parameters	33796 parameters	876 parameters
FLOPs	67008 FLOPs	74688 FLOPs

As expected, the number of trainable parameters for the QDNN is much lower than that of the CDNN because of its ability to encode a 2^n -dimensional Hilbert space into n qubits. A more direct comparison of CDNN and QDNN model complexity is FLOPs.

Floating Point Operations per Second (FLOPs) measure the computational cost of the forward pass through a DNN. For a single dense linear layer with input size M and output size N , the number of FLOPs C is

$$C = 2MN. \quad (64)$$

For the CDNN, we have the input layer ($3 \rightarrow 64$), a ReLU activation (64 FLOPs), 8 hidden layers ($64 \rightarrow 64$) and associated ReLU activations (64 FLOPs), and an output layer ($64 \rightarrow 4$). Therefore,

$$\begin{aligned} C_{\text{CDNN}} &= (C_{\text{in}} + C_{\text{ReLU}}) + 8(C_{\text{hid}} + C_{\text{ReLU}}) + C_{\text{out}} \\ &= (2 \cdot 3 \cdot 64 + 64) + 8(2 \cdot 64 \cdot 64 + 64) + 2 \cdot 64 \cdot 4 \\ &= 67008. \end{aligned} \quad (65)$$

For the QDNN, we have the preprocessing layer ($3 \rightarrow 6$ qubits), 8 Strongly Entangling Layers (6 qubits \rightarrow 6 qubits), and the postprocessing layers (6 qubits \rightarrow 64 \rightarrow 4) and a Tanh activation (64 FLOPs). Since each qubit is a two-state system and all the qubits in a layer are tensored together, the effective input and output sizes for the qubit layers are $2^6 = 64$. Therefore,

$$\begin{aligned} C_{\text{QDNN}} &= C_{\text{pre}} + 8C_{\text{SEL}} + (C_{\text{post}} + C_{\text{Tanh}}) \\ &= (2 \cdot 3 \cdot 64) + 8(2 \cdot 64 \cdot 64) \\ &\quad + (2 \cdot 64 \cdot 64 + 64 + 2 \cdot 64 \cdot 4) \\ &= 74688, \end{aligned} \quad (66)$$

which is comparable to the CDNN.

The model complexity comparison results are summarized in Table IV. These results demonstrate that the CDNN and QDNN are similar in complexity and architecture and therefore serve as a good baseline comparison of the classical and quantum approaches to CFF extraction.

2. CFF Extraction Test

Having established the architectures and complexity of the CDNN and Basic QDNN models, we now present

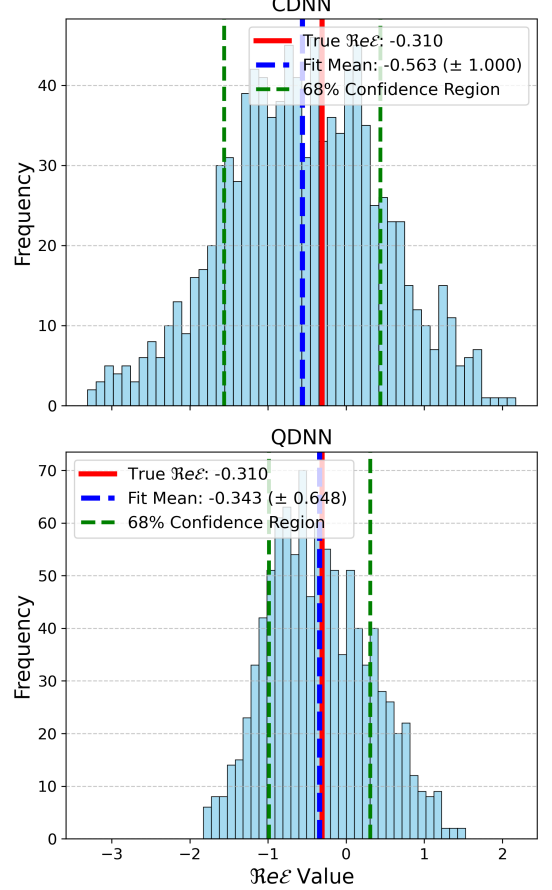
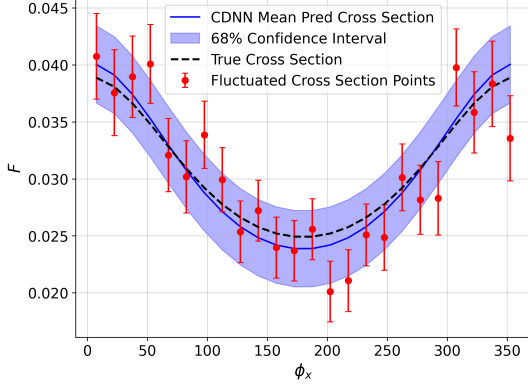


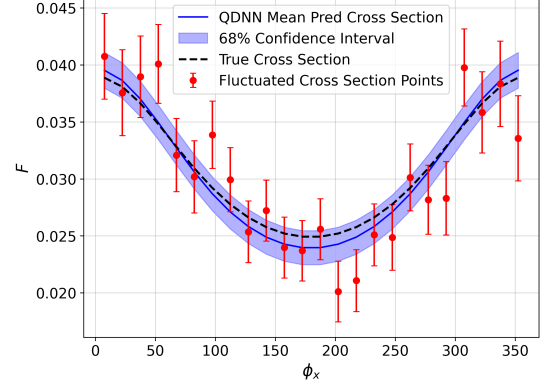
FIG. 7: Distributions of the extracted $\Re\mathcal{E}$ from noisy replicas of cross section pseudodata generated from kinematics $k = 5.75$ GeV, $Q^2 = 2.22$ GeV², $x_B = 0.333$, $t = -0.16$ GeV² (Set 144). The histograms display improved accuracy and precision by the QDNN.

the results of their performance in extracting CFFs from the pseudodata sets. Figure 7 shows representative histograms of the $\Re\mathcal{E}$ extraction from 1000 noisy replicas of the cross-section pseudodata for a fixed kinematic setting. In this case, the QDNN exhibits improvement in both accuracy (proximity to the true) and precision (width of the distribution).

To quantify overall performance, we define a reduced

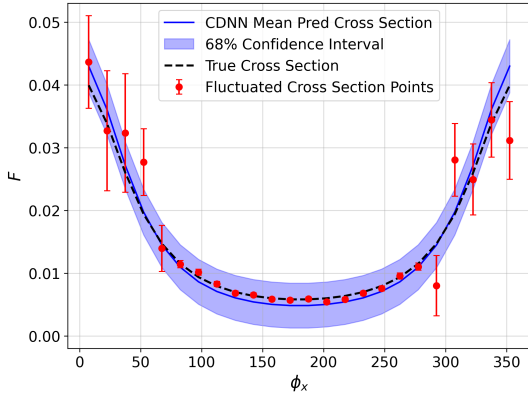


(a) CDNN

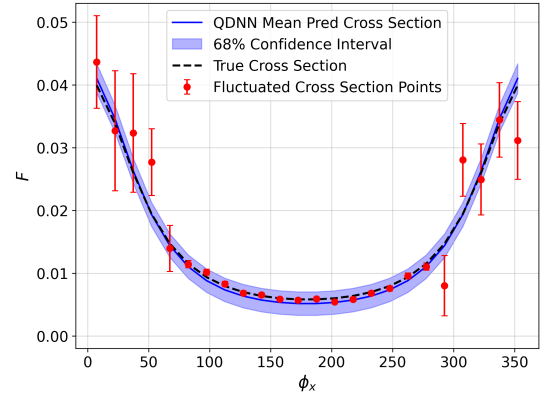


(b) QDNN

FIG. 8: Predicted cross sections from the CDNN and QDNN fits of noisy replicas of cross section pseudodata (red points) generated from kinematics $k = 8.521$ GeV, $Q^2 = 3.65$ GeV², $x_B = 0.367$, $t = -0.20459$ GeV² (Set 26).



(a) CDNN



(b) QDNN

FIG. 9: Predicted cross sections from the CDNN and QDNN fits of noisy replicas of cross section pseudodata (red points) generated from kinematics $k = 5.75$ GeV, $Q^2 = 2.48$ GeV², $x_B = 0.399$, $t = -0.45$ GeV² (Set 165). In both cases there is a small improvement in proximity to the true with a clear narrowing of the error band for the QDNN.

χ^2 metric, M_{χ^2} , as the sum of the reduced χ^2 values for each CFF across all 195 kinematic bins. A lower M_{χ^2} indicates a better fit, with a value of 4 corresponding to a perfect match. Averaging over all bins, we find $\overline{M}_{\chi^2}^{\text{CDNN}} \approx 78.97$ and $\overline{M}_{\chi^2}^{\text{QDNN}} \approx 28.18$, indicating that the QDNN outperforms the CDNN by approximately 64.3%, even without leveraging quantum-specific enhancements.

The predicted cross sections using the predicted CFFs from the CDNN and QDNN are also analyzed. Using the framework described in Section II, we compute the predicted cross sections using the extracted CFFs and compare them to the true cross section values used to generate the pseudodata. In Figs. 8 and 9, we present results for two representative kinematic bins, plotting the mean predicted cross-section values as a function of the azimuthal angle ϕ , along with their 68% confidence intervals. The true cross-section curve and fluctuated true cross-section points with simulated experimental error

from the pseudodata sets are overlaid for reference. A key observation from these figures is that the improved precision of the QDNN extraction leads to narrower confidence intervals in the predicted cross sections across all three bins due to the reduced uncertainty in the extracted CFFs. In these examples, there is also a small, observable improvement in the accuracy of the predicted cross section by the QDNN.

Understanding the sources of error is essential for robust model evaluation. A detailed analysis of the errors in the CFF extractions is necessary to fully understand and quantify the differences between QDNN and CDNN approaches. We consider four distinct error metrics: algorithmic error, methodological error, precision, and accuracy. To compute the algorithmic error, we perform the extraction on 1000 *identical* replicas of each bin and calculate the resulting spread of each CFF. Thus, algorithmic error represents error resulting from the limitations and inherent uncertainties of the extraction al-

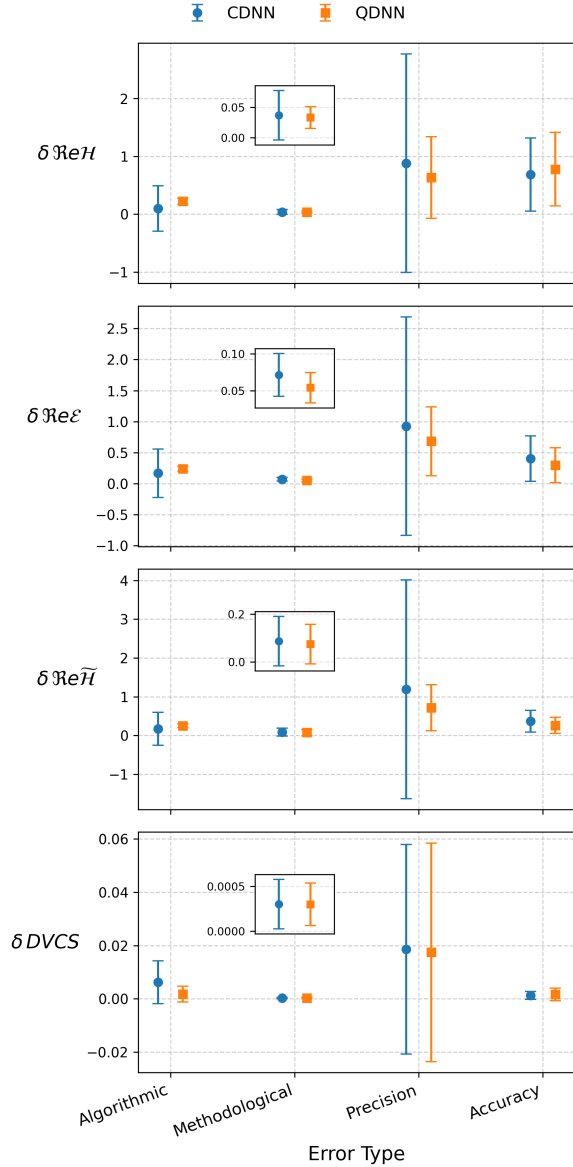


FIG. 10: Comparative error distributions of the CDNN (blue) and QDNN (orange) extraction across all kinematic bins. The points and error bars show histogram mean and error. Algorithmic error isolates uncertainty in the extraction process itself. The QDNN shows higher algorithmic error due to quantum-specific challenges, addressed in Sec. V B. Methodological error captures uncertainty arising from model assumptions.

The QDNN consistently demonstrates lower methodological error, highlighting its robustness to systematic uncertainties. Precision reflects consistency across runs, regardless of proximity to the true value.

The QDNN achieves higher precision for all CFFs, ensuring more stable and reliable extractions even when accuracy is lower. Accuracy measures how close the DNN extractions are to the true CFFs. The QDNN shows improved accuracy for $\Re \mathcal{E}$ and $\Re \tilde{H}$.

algorithm itself, rather than simulated experimental error in the data. To compute the methodological error, we introduce a spread in the parameters used to generate the CFFs (Table III) and use the generating function [Eq. (57)] to generate CFFs sampled in a domain that approximately corresponds to the spread in the original extracted CFFs. Then, the methodological error is computed as the spread of the resulting residuals from the new extractions. Methodological error represents the uncertainty arising from the choice of model parameters and assumptions used in the extraction process. By introducing a spread in the parameters used to generate the CFFs and propagating this spread through the generating function, we assess how variations in these underlying assumptions influence the extracted CFF values. This approach allows us to estimate the systematic impact of modeling choices on the final extraction results, distinguishing it from purely statistical or algorithmic uncertainties. Finally, precision and accuracy are computed using Eqs. (59) and (58), respectively. These metrics provide an evaluation of the performance of the DNNs on the original pseudodata set, with precision measuring the consistency of the extracted values across multiple replicas and accuracy reflecting the agreement between the extracted and true CFFs. For all four of these error metrics, a lower value indicates a lower error.

Figure 10 presents a comparative analysis of algorithmic error, methodological error, precision, and accuracy for the DNN-based extraction of each CFF across all 195 kinematic bins. In the plot, the absolute mean deviation from the true value is shown for each contribution as a point, while the spread in that deviation is represented by the error bar for each point. A notable improvement in the three CFFs' precision is observed with the QDNN, whereas the other error contributions remain largely comparable between the two models. The QDNN shows an improved extraction accuracy for $\Re \mathcal{E}$ and $\Re \tilde{H}$ while the CDNN performs better for $\Re \tilde{H}$ and $DVCS$. Methodological errors are fairly small in both cases, but with a narrower distribution for the QDNN, indicating a bit better robustness to variations in the model parameters used to generate the CFFs. The increase in precision from the QDNN is also evident in the predicted cross-section plots (Figs. 8 and 9) as visibly tighter confidence intervals. Overall, QDNN demonstrates improved total error performance compared to CDNN, underscoring its effectiveness in this application.

Although the QDNN outperforms the CDNN in terms of methodological error, precision, and accuracy, Fig. 10 reveals that it exhibits a higher algorithmic error for the three CFFs. This indicates that while QDNNs generally improve precision and accuracy, the simplified transformation of the CDNN into the basic QDNN introduced additional sources of uncertainty during training, leading to an overall increase in algorithmic error. Specifically, the increased algorithmic error in QDNNs stems from initialization and optimization challenges unique to quantum networks. Unlike classical models, QDNNs must respect

constraints such as unitarity and entanglement. Our implementation employs strongly entangling layers. While these are designed to capture potential quantum correlations in the data—if present—they also can enhance the model’s ability to represent higher-order nonlinearities and interference-like patterns. However, this expressiveness comes at the cost of a more complex and potentially rugged optimization landscape. Another important challenge in training QDNNs is overcoming barren plateaus, where the gradients vanish exponentially as the number of qubits increases. To mitigate this, we used small-angle initialization, sampling parameters from a narrow normal distribution. While this helps to maintain non-vanishing gradients, it also limits the search space and contributes to algorithmic error since it forces the QDNN to explore a constrained region of the parameter space in early training. This can slow down convergence and make the network more sensitive to local minima, leading to greater variability in the extracted CFFs across different replicas, manifesting as higher algorithmic error. This baseline comparison study suggests that the QDNN extraction can be further improved by refining initialization and optimization techniques and fully leveraging the quantum advantage. Building upon the insights gained from the Basic QDNN, we will now introduce the Full QDNN, which leverages quantum-specific optimizations to further enhance CFF extraction performance.

B. Leveraging the Quantum Advantage

In this section, we develop a new QDNN, which we refer to as the Full QDNN (FQDNN), that aims to optimize CFF extraction by employing quantum-specific capabilities and mitigating quantum-specific challenges (Sec. VB1). Then, we use the FQDNN to perform the same error analysis as in Sec. VA and briefly discuss the results (Sec. VB2).

1. Full QDNN Model

To systematically explore quantum-specific optimizations, we explore three new QDNN models (Models 1-3) in the Appendix, each incorporating targeted modifications designed to enhance specific aspects of the architecture with the goal of improving stability and reducing error. Our baseline model, the Basic QDNN—introduced earlier in Sec. VA—is a straightforward quantum adaptation of the CDNN. Although not fully optimized, it serves as a proof of concept for achieving a quantum advantage in CFF extraction and provides a valuable foundation for identifying potential improvements. The QDNN algorithmic error improvements observed from Models 1-3 are more comparable to the algorithmic errors from the CDNN extraction (see Fig. 10) and suggest key strategies for reducing algorithmic error and improving precision in quantum deep learning models for CFF

extraction. Specifically, by refining the entanglement structure, implementing layer-wise training, and adjusting initialization schemes, we demonstrate that targeted modifications can significantly enhance training stability and overall model reliability. Therefore, to construct our FQDNN, we incorporate all the improvements from Models 1-3, including tunable entanglement range (Model 1), layer-wise training (Model 2), and depth-scaled, larger-angle initialization (Models 2 and 3), while maintaining the baseline architecture from the Basic QDNN, including a width of 6 qubits and classical pre- and post-processing layers.

For clarity, we provide a detailed description of the architecture of the FQDNN as follows. The classical pre-processing layer is a single fully-connected linear layer that maps the 3-dimensional input (x_B, Q^2, t) to a 6-dimensional vector, matching the number of qubits in the quantum device [57]. The quantum circuit then encodes this input using angle embedding, which applies rotation gates parameterized by input features [22]. Following encoding, the circuit applies strongly entangling layers, where entanglement is controlled by a new entanglement strength hyperparameter [35]. We choose nearest-neighbor entanglement for the FQDNN [34].

Trainable weights in the quantum circuit are initialized with a depth-scaled scheme: the standard deviation of the normal distribution used for initialization is scaled as $1/\sqrt{l+1}$ for the l -th layer [58]. This encourages smaller initial angles in deeper layers, which mitigates barren plateaus by ensuring gradients are initially non-zero and preventing over-saturation [27]. The output of the quantum circuit consists of the expectation values $\langle Z \rangle$ for each qubit, forming a 6-dimensional vector [22].

This vector is then passed through a classical postprocessing layer consisting of a fully-connected linear layer with 64 hidden units and Tanh activation, followed by a final output layer mapping to the four CFFs [57]. The quantum circuit is dynamically rebuilt as the depth of the circuit gradually increases from 2 layers to 8 layers, using a factory function that generates a new quantum node with the updated number of layers [34].

To test the FQDNN, we perform the same error analysis used on Models 1-3 and display the results in Table XVIII in the Appendix. Incorporating features from Models 1-3 allows the FQDNN to perform better overall than each of the individual models, with improved algorithmic error and precision over all 4 CFFs. With these example kinematics, the FQDNN also exhibits improved methodological error for $\Re\mathcal{E}$, $\Re\tilde{\mathcal{H}}$, and $DVCS$ and improved accuracy for $\Re\tilde{\mathcal{H}}$ and $DVCS$.

2. CFF Extraction Results

We now summarize our results of the full CFF extraction from the pseudodata sets using the CDNN and FQDNN. The results of our error propagation analysis are summarized in Fig. 11. These results demon-

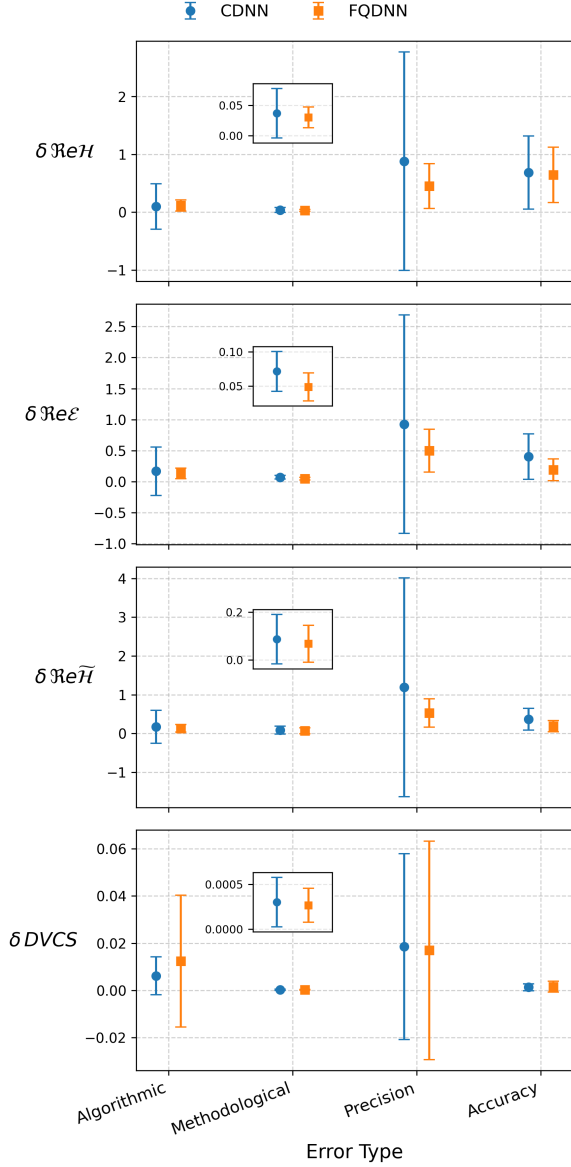
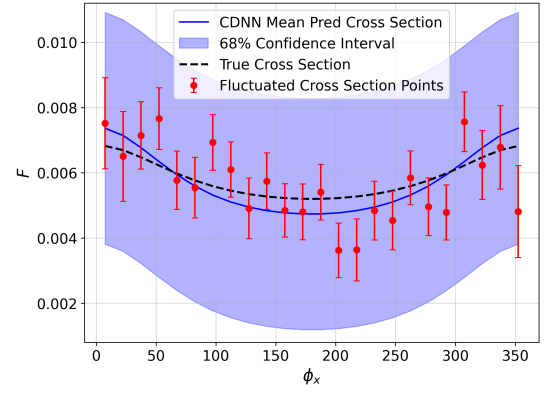


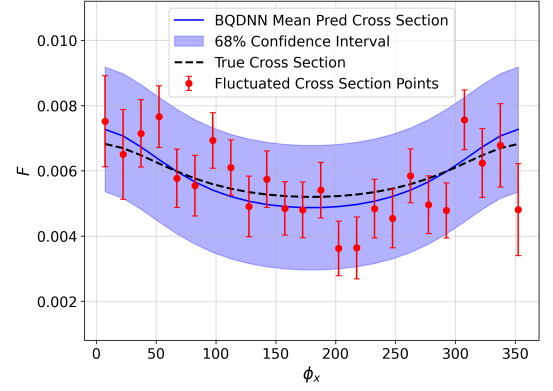
FIG. 11: Comparative error distributions of the CDNN (blue) and Full QDNN (orange) extraction across all kinematic bins. The points and error bars show histogram mean and error. These results indicate that QDNNs achieve overall lower errors in extracting CFFs when quantum-specific advantages are leveraged and quantum-specific challenges are mitigated.

strate overall improved FQDNN performance in terms of methodological error and accuracy, and superior FQDNN performance in terms of precision. The CDNN and FQDNN perform similarly in terms of algorithmic error. It is also clear that the DVCS term does not benefit from the FQDNN in comparison to the Basic QDNN. However, in terms of the predicted cross section, it is clear from the example in Fig. 12 that the FQDNN performs better than both the CDNN and BQDNN overall.

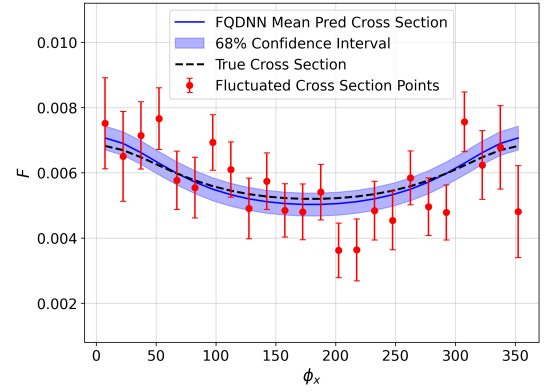
These results demonstrate that QDNNs serve as a pow-



(a) CDNN



(b) Basic QDNN



(c) Full QDNN

FIG. 12: Predicted cross sections from the CDNN, Basic QDNN, and Full QDNN fits of noisy replicas of cross section pseudodata (red points) generated from kinematics $k = 8.847$ GeV, $Q^2 = 5.36$ GeV², $x_B = 0.485$, $t = 0.50851$ GeV² (Set 48). In this example, the FQDNN exhibits a dramatic improvement from the CDNN and BQDNN in terms of proximity to the true cross section and a small improvement in accuracy.

erful tool for the extraction of CFFs from DVCS data; overall, they outperform CDNNs in terms of minimizing error, especially when the quantum architecture is fully

optimized. However, while the extracted CFFs from the FQDNN are frequently better at predicting the true cross section, the CDNN can, under certain circumstances, outperform the QDNN. This naturally leads to the question of how to determine the optimal algorithm given a particular dataset, kinematics, or error scale. To do this, we move towards developing a novel quantum qualifier metric that will allow us to predict whether a CDNN or FQDNN is better suited for a CFF extraction from experimental DVCS data with a given set of kinematics by identifying conditions under which QDNNs are expected to outperform CDNNs.

VI. DVCS QUANTUM QUALIFIER

In this section, we construct a quantum qualifier $\hat{\Xi}_{DVCS}$ tailored specifically for DVCS data. The goal of the quantum qualifier is to determine whether the CDNN or FQDNN (described in Sec. VB) should be used for the extraction of CFFs from a given set of experimental DVCS data, based solely on its functional characteristics. The quantum qualifier is designed based on CDNN and FQDNN extractions from systematically constructed pseudodata with physically realistic kinematics, CFFs, and error. Then, the quantum qualifier is tested, and in the following section (Sec. VII), it is used to perform a preliminary check to determine which algorithm (QDNN or CDNN) is optimal for that particular kinematic set for maximal extraction of CFF information.

A. Pseudodata Generation

We begin by generating pseudodata to base the DVCS quantum qualifier on. The pseudodata sets use the kinematic values from the experimental data sets, but the CFFs used to generate the cross-section values and the simulated error added to the cross-section values are systematically varied.

To begin, we first perform a baseline CFF extraction from the real experimental data described in Sec. IV using the CDNN. The purpose of this initial extraction is to obtain a range of realistic CFFs to generate the pseudodata sets for the construction of the quantum qualifier. This initial extraction is carried out on 1000 replicas of the experimental cross-section data, where each replica samples cross-section values within the experimental uncertainty for a given set of kinematics. This gives us 1000 sets of CDNN-extracted CFFs for each set of kinematics. Across all of the experimental data, most of the extracted CFFs are between -5 and 5 , which is physically reasonable.

The CFFs from this initial CDNN extraction are used to generate the pseudodata sets that we use to construct the DVCS quantum qualifier. For each of the 195 sets of kinematics, we consider five values of each of the four CFFs, evenly spaced within a 95% confidence interval of

the extracted CFFs. We also consider four error values for each cross-section point: 0 , $0.5\sigma_F$, $1\sigma_F$, and $2\sigma_F$, where σ_F is the true experimental error of the cross-section point. Therefore, for each of the 195 sets of kinematics, we generate $5^4 \cdot 4 = 2500$ replicas with varying, physically-realistic CFFs and error. This provides us with a comprehensive collection of pseudodata sets on which to construct the quantum qualifier.

B. Quantum Qualifier

In order to construct the DVCS quantum qualifier $\hat{\Xi}_{DVCS}$, we first define the quantum outperformance metric for DVCS, Ξ_{DVCS} , which $\hat{\Xi}_{DVCS}$ is intended to estimate. The quantum outperformance metric for DVCS is very similar to the metric we used to measure quantum outperformance for regression in Sec. IIIB; we first define a metric M_{DVCS} to assess the quality of a DNN fit:

$$M_{DVCS} = \int_{\phi_{\min}}^{\phi_{\max}} |F_{\text{DNN}}(\phi) - F_{\text{true}}(\phi)| d\phi, \quad (67)$$

where $F_{\text{DNN}}(\phi)$ is the predicted cross section curve from the DNN-extracted CFFs and $F_{\text{true}}(\phi)$ is the true cross section curve (with no experimental error). Most of the pseudodata sets have $\phi_{\min} = 7.5^\circ$ and $\phi_{\max} = 352.5^\circ$. Then, the quantum outperformance Ξ_{DVCS} is defined as

$$\Xi_{DVCS} = M_{DVCS}^{\text{CDNN}} / M_{DVCS}^{\text{QDNN}} - 1, \quad (68)$$

so $\Xi_{DVCS} > 0$ means that the QDNN achieves a better fit, and vice versa. The magnitude of Ξ_{DVCS} indicates the extent to which the better DNN outperforms.

We perform the CFF extraction on the pseudodata sets described in the previous section using the CDNN and FQDNN (Sec. VB), which gives us a quantum outperformance value for each of the 2500 replicas of each of the 195 sets of kinematics. Following the example of Sec. IIIB, we then examine the Ξ_{DVCS} -dependence on the five established function characteristics: nonlinearity, frequency complexity, fractal dimension, mutual information, and Fourier transform complexity. Unlike the bulky quantum qualifier expression in Eq. (55), we want to construct a relatively simple expression that serves as a useful indicator for which DNN to use, so we only consider the strongest correlations. Additionally, since both the CDNN and FQDNN are optimized, the quantum qualifier $\hat{\Xi}_{DVCS}$ is not dependent on the number of epochs n . We find that Ξ_{DVCS} has a meaningful correlation with nonlinearity (\mathfrak{N}), with a linear fit $\Xi_{DVCS} = -1.19\mathfrak{N} + 0.65$. This indicates that a higher nonlinearity results in lower QDNN outperformance.

The magnitude of the experimental error significantly influences the potential for quantum advantage. To quantify this in the qualifier, we examine the explicit dependence of Ξ_{DVCS} on the relative error. We define the average scaled error $\bar{\epsilon}_s$ as the mean of the ratio

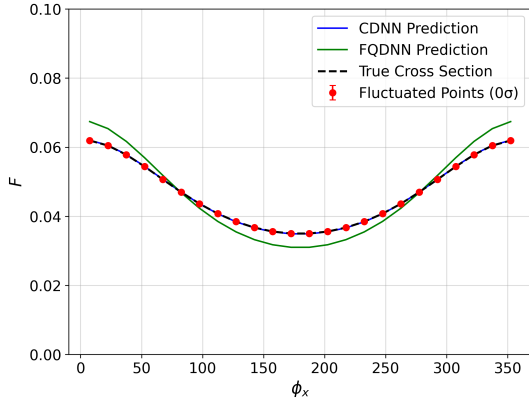
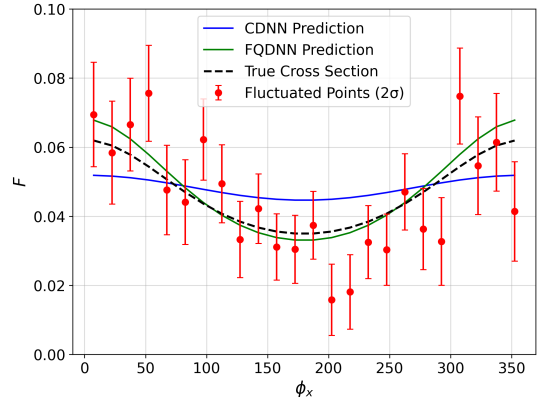
(a) $0\sigma_F$ experimental error(b) $2\sigma_F$ experimental error

FIG. 13: Predicted cross section from the CDNN and QDNN fits of cross section pseudodata (red points) generated from kinematics $k = 5.75$ GeV, $Q^2 = 2.012$ GeV², $x_B = 0.378$, $t = -0.192$ GeV² and CFFs $\Re\mathcal{E} \approx -1.229$, $\Re\mathcal{H} \approx -1.360$, and $DVCS = 0.0114$. This example comparison illustrates the general trend of increased quantum outperformance Ξ_{DVCS} with greater experimental error.

$s\sigma_{F,i}/F_{i,r}$ over all valid kinematic points i and replicas r , where s is the error scaling factor (e.g., $s = 0, 0.5, 1, 2$), $\sigma_{F,i}$ is the experimental uncertainty at point i (identical across replicas), and $F_{i,r}$ is the corresponding cross section value:

$$\bar{\epsilon}_s(k, Q^2, x_B, t) = \frac{1}{N} \sum_{i,r} \frac{s\sigma_{F,i}}{F_{i,r}}, \quad (69)$$

with N the total number of (i, r) pairs. Varying $\bar{\epsilon}_s$ across the pseudodata sets from 0 to 0.6 allows us to study the impact of increasing experimental uncertainty. We find a strong positive correlation between Ξ_{DVCS} and $\bar{\epsilon}_s$, well-approximated by the linear relation $\Xi_{DVCS} = 2.00\bar{\epsilon}_s - 0.66$.

This trend is illustrated in Fig. 13. When there is no experimental error, the CDNN achieves a nearly perfect fit (Fig. 13a), whereas the FQDNN underperforms slightly. However, under high experimental uncertainty (Fig. 13b), the CDNN performance degrades significantly, while the FQDNN remains robust—highlighting the increased quantum outperformance with increasing error.

The DVCS quantum qualifier, combining Ξ_{DVCS} dependencies on $\bar{\epsilon}_s$ and \Re weighted by correlation strength, is given by:

$$\hat{\Xi}_{DVCS} = 1.98\bar{\epsilon}_s - 0.132\Re - 0.583. \quad (70)$$

A positive $\hat{\Xi}_{DVCS}$ suggests the QDNN will likely outperform, with its magnitude indicating the degree of outperformance. While $\hat{\Xi}_{DVCS}$ guides predictions of quantum advantage, it does not precisely determine Ξ_{DVCS} , which depends on data structure and kinematics. A linear fit of $\Xi_{DVCS} = 1.0004\hat{\Xi}_{DVCS} - 0.0042$ ($R^2 = 0.42$), based on average $\hat{\Xi}_{DVCS}$ across kinematic sets and noise level s (excluding extreme outliers), confirms approximate agreement with quantum outperformance. This

simple utility provides the means of checking experimental data sets to determine which algorithm type would perform best and can be used on past or future experimental data. With the quantum qualifier defined and its predictive power established, we apply our optimized CFF extraction method to real experimental data for practical validation.

VII. OPTIMIZED CFF EXTRACTION FROM EXPERIMENTAL DATA

This section demonstrates the practical application of the DVCS quantum qualifier $\hat{\Xi}_{DVCS}$ for optimized CFF extraction on a subset of real experimental data (see Sec. IV), validating our QDNN approach in a realistic setting beyond pseudodata. We select a subset where $\hat{\Xi}_{DVCS}$ predicts quantum outperformance in most kinematics to evaluate the quantum advantage. This subset has enough data for a good demonstration, but with a variety of experimental errors. A future paper will apply a $\hat{\Xi}_{DVCS}$ -guided CFF extraction to the full dataset using CDNN and FQDNN as indicated by the qualifier.

In Sec. VII A, we describe generating realistic pseudodata from the initial CDNN extraction of experimental data (Sec. VI A). In Sec. VII B, we tune CDNN and FQDNN on this pseudodata to extract physically realistic CFFs and assess the DVCS quantum qualifier's effectiveness. Finally, in Sec. VII C, we perform a $\hat{\Xi}_{DVCS}$ -guided CFF extraction on the selected experimental data subset and present the results.

TABLE V: The parameters used in Eq. (57) to generate the realistic pseudodata set, fitted from the initial CDNN extraction in Sec. VIA.

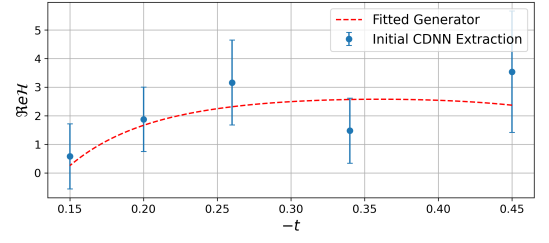
CFFs	a	b	c	d	e	f
$\Re\mathcal{H}$	-8.13	1.82	35.26	25.37	6.26	3.20
$\Re\mathcal{E}$	6.92	-5.64	0.81	0.98	4.03	49.71
$\Re\tilde{\mathcal{H}}$	-8.51	1.72	31.11	22.49	6.09	4.77
DVCS	0.45	-0.45	4.40	2.91	0.13	0.08

A. Realistic Pseudodata Generation

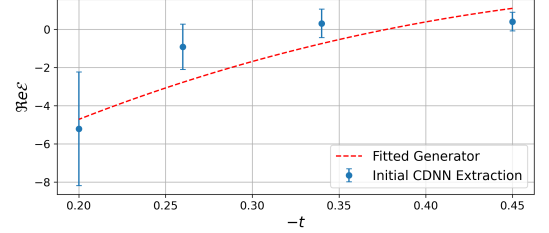
We choose to examine a specific subset of the experimental data (Sets 108 to 175) that has kinematics $k = 5.75$ GeV, Q^2 from 1.79 GeV² to 3.77 GeV², x_B from 0.244 to 0.475 , and t from -0.11 GeV² to -0.45 GeV². This subset selects 1145 points in a physically relevant region of phase space covered by JLab experiments (Sec. IV), where the DVCS cross-section data has a range of experimental errors.

Realistic pseudodata is required for the testing and optimization phase. In order to generate the pseudodata in this range of kinematics, we begin by modeling the underlying CFFs as smooth functions of the kinematic variables x_B and t . Specifically, we fit the parameters a, b, c, d, e, f of the *basic* generating function, Eq. (57), to the CFFs obtained from the initial CDNN extraction described in Sec. VIA, which provides pointwise estimates of the true CFFs at each kinematic setting. The fit is performed using a non-linear least squares method that minimizes the squared difference between the predicted values of the generating function and the CDNN-extracted CFFs across all kinematic points in the subset. The resulting optimized parameter values are shown in Table V. To validate the quality of the fit, Fig. 14 compares the fitted generating function predictions with the CDNN-extracted CFFs, which demonstrates that the fitted functions capture the general trend and magnitude of each CFF across the kinematic region.

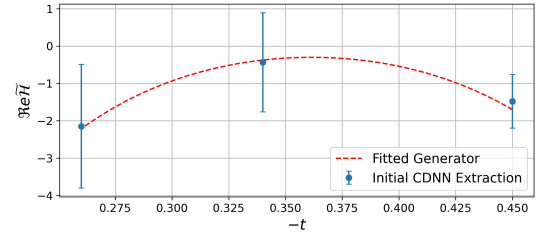
Using the improved generating function as a stand-in for the “true” kinematic dependence of the CFFs, we construct a new set of realistic pseudodata. Following the procedure in Sec. IV A, we use the fitted function to generate the CFFs for each experimental kinematic setting. These CFFs are then used to compute the DVCS cross section at each ϕ point. To simulate realistic measurement uncertainties, we add Gaussian noise to each cross-section value based on the established experimental error. Finally, for each kinematic point, we generate 1000 replicas of noisy cross-section data by resampling within the experimental uncertainty. These realistic pseudodata sets are then used for the tuning and evaluation of the DNNs.



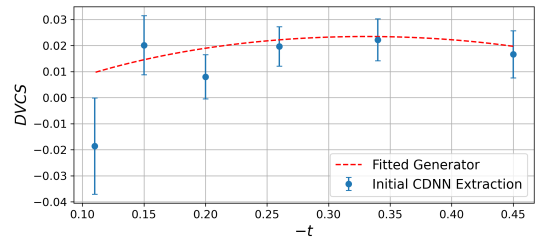
(a) $\Re\mathcal{H}$ vs $-t$ with $x_B = 0.275$



(b) $\Re\mathcal{E}$ vs $-t$ with $x_B = 0.365$



(c) $\Re\tilde{\mathcal{H}}$ vs $-t$ with $x_B = 0.399$



(d) DVCS vs $-t$ with $x_B = 0.244$

FIG. 14: Example comparisons between the initial CDNN-extracted CFFs (blue with error bars) and the CFFs produced from the generating function [Eq. (57)] using the fitted parameters in Table V (red). The CFFs are plotted against $-t$ for select values of x_B in the subset of all experimental data specified in the text.

B. Realistic Pseudodata Extraction

We perform both CDNN and FQDNN extractions on the realistic pseudodata sets to optimize the performance of the deep neural networks for application to real experimental measurements. This optimization is achieved by tuning key hyperparameters of each network. For both models, the number of training epochs and the learning rate are varied, while for the FQDNN specifically,

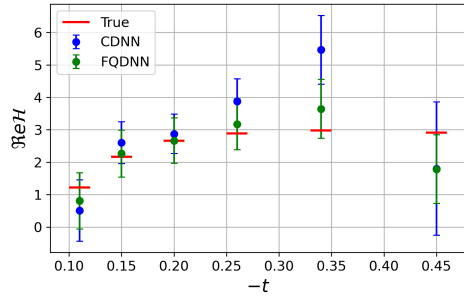
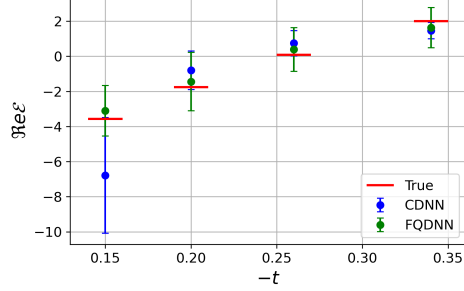
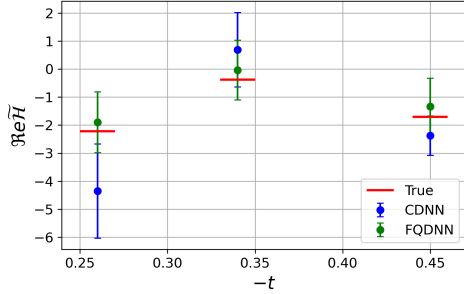
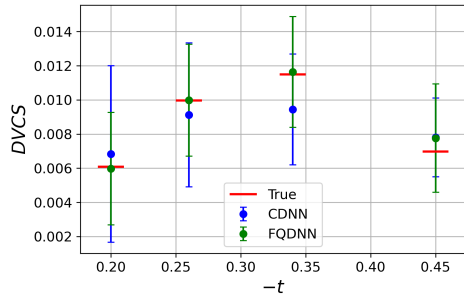
(a) $\text{Re}\mathcal{H}$ vs $-t$ with $x_B = 0.244$ (b) $\text{Re}\mathcal{E}$ vs $-t$ with $x_B = 0.304$ (c) $\text{Re}\tilde{\mathcal{H}}$ vs $-t$ with $x_B = 0.399$ (d) $DVCS$ vs $-t$ with $x_B = 0.335$

FIG. 15: Example comparisons of CFFs extracted by the tuned CDNN and FQDNN from realistic pseudodata. The CDNN results are shown in blue, the FQDNN results are shown in green, and the true CFFs are shown as red lines. These plots reflect the improved FQDNN performance in terms of accuracy and precision as predicted by the DVCS quantum qualifier.

additional quantum-specific parameters—such as entanglement strength and input normalization—are systematically scanned. These hyperparameters are adjusted to maximize both the accuracy, defined as the agreement with the true CFFs used to generate the pseudodata, and the precision, defined as the stability of the extracted CFFs across noisy replica datasets.

The quantum qualifier $DVCS \hat{\Xi}_{DVCS}$ [Eq. (70)] indicates that the FQDNN should outperform nearly all (96%) of the pseudodata sets. This is confirmed by the realistic pseudodata extraction, which shows overwhelming quantum outperformance. In Fig. 15, we plot example comparisons of the extracted CFFs by the tuned CDNN and FQDNN. As predicted by the DVCS quantum qualifier, the FQDNN demonstrates improved accuracy and precision across the entire range of kinematic values covered by the realistic pseudodata sets, effectively capturing the trend in the CFFs.

C. Experimental Data Extraction

Informed by the DVCS quantum qualifier $\hat{\Xi}_{DVCS}$ and the demonstrated quantum advantage in the realistic pseudodata extraction, we apply the optimized FQDNN to perform the CFF extraction on the real experimental data subset. A comprehensive summary of the mean values and associated uncertainties (standard deviations) of the FQDNN-extracted CFFs is provided in Table XIX in the Appendix.

To visualize these results, we present surface plots of the extracted CFFs plotted as functions of the kinematic variables x_B and $-t$ in Fig. 16. To create these plots, we applied a multi-step interpolation and smoothing strategy to visualize the mean predicted FQDNN-extracted CFFs across a continuous kinematic landscape (this can also be performed with either a QDNN or CDNN). We first generated a uniform two-dimensional mesh-grid in $(x_B, -t)$ space with 80 points in each direction, spanning the kinematic domain of the experimental data subset. Then, generating discrete data points by averaging over the FQDNN-extracted CFFs for all the replicas of a given $(x_B, -t)$ point, we interpolated the discrete FQDNN predictions onto this grid by estimating values on the mesh by forming triangles between known data points and linearly interpolating within those simplices. However, since the experimental data is not uniformly distributed, we handled sparsely sampled regions by performing a secondary pass of nearest-neighbor interpolation to fill gaps where linear interpolation returned undefined values. To reduce local noise and improve the visual coherence of the surfaces, we further applied a Gaussian filter of standard deviation 6.0 to the interpolated data, which gently smoothed out high-frequency fluctuations while maintaining the overall structure and trends of the extracted CFFs.

For consistency checks, we compare our resulting QDNN fit to the KM15 model [59], a modern global fit

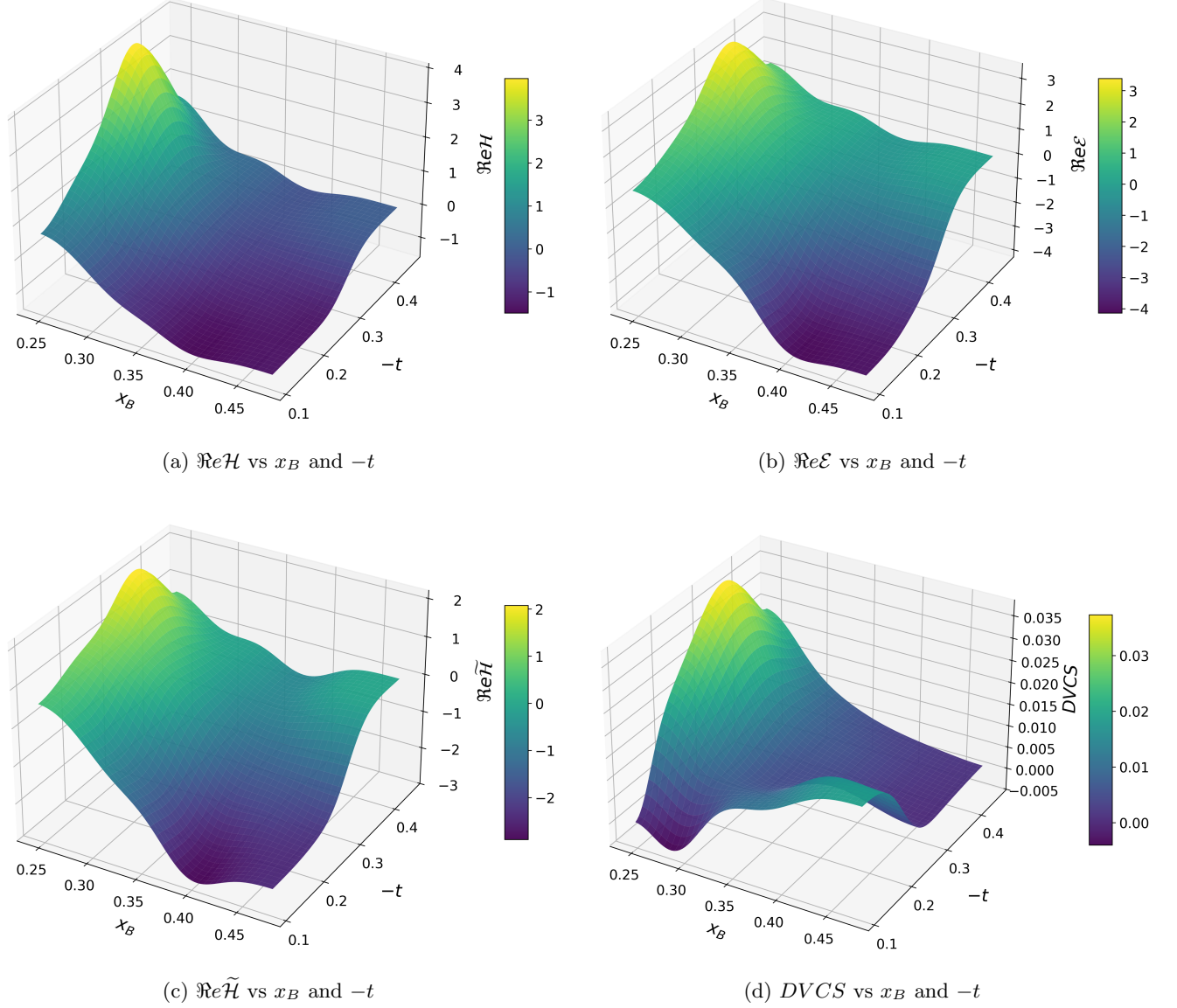


FIG. 16: Three-dimensional surface plots of (a) $\text{Re}\mathcal{H}$ vs. x_B and $-t$, (b) $\text{Re}\mathcal{E}$ vs. x_B and $-t$, (c) $\text{Re}\tilde{\mathcal{H}}$ vs. x_B and $-t$, and (d) $DVCS$ vs. x_B and $-t$, generated using a multi-step interpolation and smoothing strategy applied to discrete FQDNN predictions on a uniform mesh-grid in the $(x_B, -t)$ kinematic space, with linear interpolation within triangular simplices formed by known data points. Each plot shows the average prediction over the ensemble of trained replicas, highlighting the overall trend extracted from the data.

for DVCS that parametrizes the dominant CFFs using a flexible GPD ansatz. It builds on earlier KM10b [60] and KMM12b [61] fits and incorporates updated DVCS cross section and asymmetry data, including the earlier, but incomplete data of same measurements from Hall A E07-007 and E00-110 [62] and CLAS Hall B e1-DVCS1 [63, 64] as what is in the Table II. The model includes both H and E GPDs, with a simplified functional form that allows for control over t -dependence and skewness effects. It assumes factorized t -dependence and parametrizes the GPDs using Regge-inspired profiles and a spectral repre-

sentation consistent with polynomiality constraints. The KM15 fit reveals that the skewness effect in GPD H is small, and the t -dependence of E is flatter than that of H , aligning with expectations from dispersion relations. The model is constrained by experimental observables through Fourier harmonics of the cross section, with sensitivity enhanced by weighting techniques. Fig. 17 shows that the our FQDNN replica mean as the blue line is consistency within 1σ error bands with the KM15 model (red line) for $\text{Re}\mathcal{E}$, and $\text{Re}\tilde{\mathcal{H}}$, but deviates with a clear increasing trend in $-t$ for $\text{Re}\mathcal{H}$. Further analysis on the full

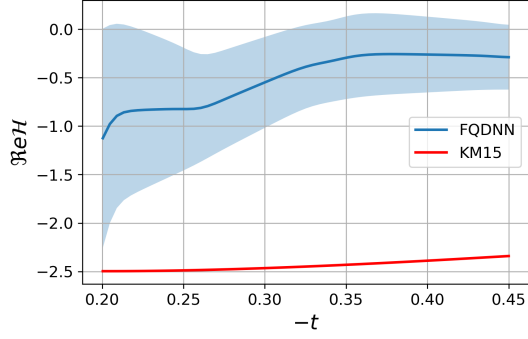
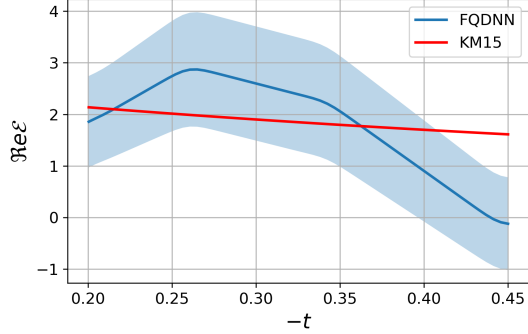
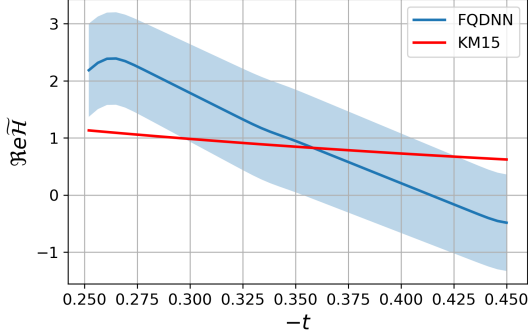
(a) $\Re\mathcal{H}$ vs $-t$ with $x_B = 0.365$ (b) $\Re\mathcal{E}$ vs $-t$ with $x_B = 0.275$ (c) $\Re\tilde{\mathcal{H}}$ vs $-t$ with $x_B = 0.305$

FIG. 17: Example comparisons between the FQDNN-extracted CFFs from the real experimental data subset and the KM15 prediction. The FQDNN mean is shown as the blue line with shaded 1σ error band, and the KM15 curve is shown in red.

dataset would be required to make a broader comparison, which will be addressed in future work. The framework and software used in this analysis can be found at the UVA Spin Physics GitHub [65].

VIII. CONCLUSION

We performed the first-ever extraction of CFFs from experimental data using a QDNN architecture implemented with parameterized quantum circuits and provided a comparative pseudodata study of CFF extraction using both CDNNs and QDNNs within a consistent theoretical and computational framework. By employing the BKM10 formalism and training on pseudodata reflecting experimental uncertainties, we demonstrated that QDNNs can outperform CDNNs in a CFF parameter extraction in particular cases. QDNNs showed particular advantages in scenarios with larger experimental errors, high-dimensional input spaces, and complex functional relationships, conditions relevant to real-world DVCS data analysis.

These results demonstrate that QDNNs can enhance both the precision and robustness of CFF extraction for a majority of cases. QDNNs may also provide a pathway to capture quantum interference effects and hidden correlations that are difficult for classical architectures to effectively exploit, but more analysis is required in future work. The construction of a data-driven quantum qualifier (outperformance estimator) suggests that the advantage of QDNNs can be anticipated based on measurable characteristics of the input data, such as nonlinearity and experimental error. This provides a means to check the data as a function of kinematics to test whether a CDNN or QDNN would provide an optimal extraction. Future extractions may use a quantum qualifier to determine that different datasets benefit from different algorithms. The method of constructing a quantum qualifier can be used for any data type and may prove beneficial in further hadronic physics investigations.

As quantum hardware continues to mature, the integration of QDNNs into experimental pipelines may enable more accurate and less biased determinations of hadronic structure. Future work will focus on scaling to full eight-parameter extractions, incorporating polarized observables, and exploring the quantum advantage in more detailed systematic studies. The continued development of quantum-enabled analysis tools may open new avenues for precision QCD phenomenology and the extraction of partonic information from complex scattering processes.

ACKNOWLEDGMENTS

The Deep Neural Network models used in this work were trained using the University of Virginia's high-performance computing cluster, Rivanna. The authors acknowledge Research Computing at the University of Virginia for providing computational resources and technical support that have contributed to the results reported in this publication. URL: <https://rc.virginia.edu>. This work was supported by the DOE contract DE-FG02-96ER40950.

Appendix A: Additional Information

1. Regression Target Functions

The following six functions were used as target functions in the quantum regression example presented in Sec. III B 1. These functions were chosen to span a range of nonlinear behaviors and complexity levels in order to illustrate the performance differences between classical and quantum neural network models.

$$y = \cos 4x \tag{A1}$$

$$y = \sin x^3 + \cos 2x^2 + \sin 4x \tag{A2}$$

$$y = \sin 5x^3 + \cos 10x^2 + \sin 20x \tag{A3}$$

$$y = \sin(x^3 + 5 \sin 2x) + \cos(2x^2 + 3 \cos x) + \sin(4x + \cos 3x) \tag{A4}$$

$$y = \sin e^x + \cos e^{2x} + \sin e^{3x} \tag{A5}$$

$$y = \sin(\pi x) \cos(\pi \sin x^2) + \sin(\pi \cos x^2). \tag{A6}$$

2. Improved QDNN Models

Here, we discuss three QDNN models, Models 1-3, that each add one quantum enhancement to the Basic QDNN in Sec. V A to construct the Full QDNN in Sec. V B. Model 1 modifies the strongly entangling layers by adding an entanglement range parameter, limiting interactions to nearest neighbors in some cases rather than fully entangling all qubits at every layer. This aims to balance expressivity and stability, reducing excessive parameter correlations that can destabilize optimization. Model 2 focuses on addressing the barren plateau problem, a QDNN-unique issue characterized by gradients that vanish exponentially as the circuit depth increases. To mitigate this, Model 2 employs layerwise training, where the network begins with a shallow quantum circuit and progressively increases the number of layers over training. Additionally, it introduces depth-scaled initialization, ensuring that each layer's parameter magnitudes decrease as depth increases. This prevents excessive parameter magnitudes in deeper layers while maintaining trainable gradients throughout optimization. Model 3 refines the small-angle initialization used in the Basic QDNN, which is already known to help prevent barren plateaus at initialization but may overly restrict the search space, leading to increased error. Instead of reducing the initial weight magnitudes across layers, Model 3 rescales small-angle initialization to maintain better trainability without completely restricting parameter exploration.

To test these new models, we perform the CFF extraction on 1000 noisy replicas of Set 144 (see Figs. 7) using each of these four models and display the algorithmic error results in Table XVIII. Comparing the results of the Basic QDNN with Fig. 10, we observe that the errors for this kinematic bin align relatively well with the average errors of the extracted CFFs across all bins. Performing the extraction with the improved QDNN models, the algorithmic error and precision improve significantly for all three models. Table XVIII indicates that Model 1 produces the lowest algorithmic errors for $\Re\mathcal{H}$, $\Re\mathcal{E}$, and $\Re\tilde{\mathcal{H}}$, while Model 2 produces the lowest algorithmic error for $DVCS$. The improved precision follows a similar pattern. In this example, we find that these new models significantly improve accuracy and methodological error for $\Re\tilde{\mathcal{H}}$, but there is no overall trend for these two metrics.

3. Tables

This part of the appendix contains supplementary tables referenced in the main text. Each table includes its own caption describing the contents, and all are discussed in further detail where they are referenced in the article.

TABLE VI: Regression metric M_{reg} values for CDNN regression on 100 data points generated from the target functions [Eqs. (A1)-(A6)] with 0.1σ noise level.

Number of epochs	Eq. (A1)	Eq. (A2)	Eq. (A3)	Eq. (A4)	Eq. (A5)	Eq. (A6)
10	3.818	5.373	5.929	6.164	6.921	3.857
50	2.348	4.272	5.818	4.592	4.688	3.166
100	1.700	3.670	5.524	3.183	3.841	2.980
250	0.249	1.790	4.784	2.286	3.277	1.366
500	0.382	1.162	4.345	1.879	3.295	0.922

TABLE VII: Regression metric M_{reg} values for QDNN regression on 100 data points generated from the target functions [Eqs. (A1)-(A6)] with 0.1σ noise level.

Number of epochs	Eq. (A1)	Eq. (A2)	Eq. (A3)	Eq. (A4)	Eq. (A5)	Eq. (A6)
10	3.151	4.603	5.877	4.490	4.350	3.416
50	0.183	2.859	5.790	3.310	3.929	2.183
100	0.191	2.335	5.682	1.833	3.604	1.616
250	0.204	2.165	5.576	1.291	3.341	1.589
500	0.209	0.975	5.462	1.171	3.289	0.433

TABLE VIII: Regression metric M_{reg} values for the CDNN regression on 100 data points generated from the target functions [Eqs. (A1)-(A6)] with 0.25σ noise level.

Number of epochs	Eq. (A1)	Eq. (A2)	Eq. (A3)	Eq. (A4)	Eq. (A5)	Eq. (A6)
10	3.824	5.373	5.928	6.164	6.921	3.859
50	2.259	4.242	5.772	4.624	4.705	3.137
100	1.937	3.689	5.531	3.065	3.868	3.007
250	0.554	2.754	5.029	2.244	3.410	1.666
500	0.622	1.572	4.686	2.077	3.441	1.188

TABLE IX: Regression metric M_{reg} values for the QDNN regression on 100 data points generated from the target functions [Eqs. (A1)-(A6)] with 0.25σ noise level.

Number of epochs	Eq. (A1)	Eq. (A2)	Eq. (A3)	Eq. (A4)	Eq. (A5)	Eq. (A6)
10	3.697	4.620	5.964	4.503	4.301	3.438
50	0.388	2.978	5.748	3.337	4.064	3.030
100	0.444	2.382	5.698	2.030	3.800	1.833
250	0.445	1.642	5.613	1.658	3.518	1.081
500	0.581	1.400	5.493	1.455	3.582	0.946

TABLE X: Regression metric M_{reg} values for the CDNN regression on 100 data points generated from the target functions [Eqs. (A1)-(A6)] with 1σ noise level.

Number of epochs	Eq. (A1)	Eq. (A2)	Eq. (A3)	Eq. (A4)	Eq. (A5)	Eq. (A6)
10	3.865	5.371	5.923	6.164	6.922	3.881
50	3.431	4.228	5.711	4.940	4.905	3.663
100	2.593	3.500	5.602	3.707	4.515	3.459
250	2.633	3.842	5.855	3.596	4.633	2.985
500	2.215	3.390	5.528	3.015	4.429	2.904

TABLE XI: Regression metric M_{reg} values for the QDNN regression on 100 data points generated from the target functions [Eqs. (A1)-(A6)] with 1σ noise level.

Number of epochs	Eq. (A1)	Eq. (A2)	Eq. (A3)	Eq. (A4)	Eq. (A5)	Eq. (A6)
10	3.697	4.815	5.913	4.785	5.008	3.633
50	1.453	3.352	5.905	3.906	4.611	3.508
100	1.661	3.069	5.781	3.430	4.480	3.270
250	2.030	2.907	5.778	3.007	4.449	2.464
500	2.635	3.341	4.832	3.222	4.471	3.052

TABLE XII: Function characteristic data [nonlinearity (\mathfrak{N}), frequency complexity (Φ), fractal dimension (\mathfrak{D}), mutual information (\mathfrak{M}), and Fourier transform complexity (\mathfrak{F})] for regression target functions [Eqs. (A1)-(A6)] with 0.1σ noise level.

Function characteristic	Eq. (A1)	Eq. (A2)	Eq. (A3)	Eq. (A4)	Eq. (A5)	Eq. (A6)
\mathfrak{N}	0.982	0.995	0.996	0.939	0.775	0.983
Φ	26	29	36	27	25	28
\mathfrak{D}	1.637	1.491	1.679	1.488	1.525	1.531
\mathfrak{M}	0.648	0.762	0.504	0.833	0.784	0.622
\mathfrak{F}	5218.538	12459.751	13568.363	14724.023	18429.203	6100.399

TABLE XIII: Function characteristic data for regression target functions with 0.25σ noise level.

Function characteristic	Eq. (A1)	Eq. (A2)	Eq. (A3)	Eq. (A4)	Eq. (A5)	Eq. (A6)
\mathfrak{N}	0.986	0.994	0.994	0.942	0.778	0.983
Φ	31	31	36	28	25	30
\mathfrak{D}	1.618	1.533	1.684	1.518	1.547	1.553
\mathfrak{M}	0.667	0.607	0.453	0.752	0.791	0.625
\mathfrak{F}	5821.253	12971.771	13408.041	14705.103	17651.770	6016.843

TABLE XIV: Function characteristic data for regression target functions with 1σ noise level.

Function characteristic	Eq. (A1)	Eq. (A2)	Eq. (A3)	Eq. (A4)	Eq. (A5)	Eq. (A6)
\mathfrak{N}	0.997	0.997	1.000	0.963	0.879	0.977
Φ	33	35	36	29	33	26
\mathfrak{D}	1.609	1.638	1.715	1.517	1.586	1.665
\mathfrak{M}	0.468	0.458	0.497	0.541	0.585	0.485
\mathfrak{F}	14419.142	22150.011	27217.273	24568.751	32359.330	15787.680

TABLE XV: Slopes of linear regressions on the quantum outperformance Ξ against the function characteristics for DNN target function regression. The approximate range in the function characteristics, the average slopes across the different epochs, and the average change in Ξ over the function characteristic domain are reported.

	0.75 to 1	25 to 35	1.45 to 1.75	0.45 to 0.85	5000 to 35000
Epochs	\mathfrak{N}	Φ	\mathfrak{D}	\mathfrak{M}	\mathfrak{F}
10	-2.43	-0.0386	-1.69	1.12	7.06×10^{-6}
50	0.209	-0.0257	-1.89	0.725	-8.55×10^{-6}
100	1.36	-0.0327	-2.66	0.87	-3.04×10^{-5}
250	0.715	-0.0115	-1.26	0.379	-5.59×10^{-6}
500	0.746	-0.0476	-1.64	1.1	-2.26×10^{-5}
Average	0.12	-0.0312	-1.83	0.839	-1.20×10^{-5}
Average $\Delta\Xi$ over domain	0.03	-0.312	-0.549	0.337	-0.36

TABLE XVI: R^2 values of linear regressions on the quantum outperformance Ξ against the function characteristics for DNN target function regression. The average R^2 values across the different epochs are reported.

Epochs	\mathfrak{N}	Φ	\mathfrak{D}	\mathfrak{M}	\mathfrak{F}
10	0.829	0.573	0.384	0.524	0.079
50	0.008	0.306	0.596	0.267	0.12
100	0.104	0.155	0.368	0.13	0.467
250	0.032	0.023	0.096	0.027	0.022
500	0.022	0.246	0.102	0.144	0.228
Average	0.199	0.261	0.309	0.218	0.183

TABLE XVII: Parameters for the double-summation expression of $\hat{\Xi}$ from Eq. (55).

Coefficient	Value	Variable X_j	Power of n
α	0.0101	exp. prefactor	—
β_{10}	-1.17	$\mathfrak{N} - 0.25$	n^0
β_{11}	0.0163	$\mathfrak{N} - 0.25$	n^1
β_{12}	-2.65×10^{-5}	$\mathfrak{N} - 0.25$	n^2
β_{20}	-0.0222	$\Phi - 24.5$	n^0
β_{21}	2.82×10^{-4}	$\Phi - 24.5$	n^1
β_{22}	-1.40×10^{-6}	$\Phi - 24.5$	n^2
β_{23}	3.33×10^{-9}	$\Phi - 24.5$	n^3
β_{24}	-3.14×10^{-12}	$\Phi - 24.5$	n^4
β_{30}	-1.10	$\mathfrak{D} - 0.95$	n^0
β_{31}	5.39×10^{-3}	$\mathfrak{D} - 0.95$	n^1
β_{32}	-9.88×10^{-6}	$\mathfrak{D} - 0.95$	n^2
β_{33}	7.96×10^{-9}	$\mathfrak{D} - 0.95$	n^3
β_{34}	-4.06×10^{-12}	$\mathfrak{D} - 0.95$	n^4
β_{40}	0.548	$\mathfrak{M} + 0.05$	n^0
β_{41}	-6.57×10^{-3}	$\mathfrak{M} + 0.05$	n^1
β_{42}	3.05×10^{-5}	$\mathfrak{M} + 0.05$	n^2
β_{43}	-6.81×10^{-8}	$\mathfrak{M} + 0.05$	n^3
β_{44}	6.05×10^{-11}	$\mathfrak{M} + 0.05$	n^4
β_{50}	-5.97×10^{-7}	$\mathfrak{F} - 4999.5$	n^0
β_{51}	-1.48×10^{-8}	$\mathfrak{F} - 4999.5$	n^1
β_{52}	2.27×10^{-11}	$\mathfrak{F} - 4999.5$	n^2
β_{53}	-2.39×10^{-14}	$\mathfrak{F} - 4999.5$	n^3
β_{54}	2.03×10^{-17}	$\mathfrak{F} - 4999.5$	n^4

TABLE XVIII: The QDNN error contributions are listed for the Basic QDNN, Models 1-3, and Full QDNN for each CFF and DVCS term. The Basic QDNN is the baseline model used for the full extraction in Sec. V, Models 1-3, described in the Appendix, are refined models aimed to take advantage of quantum effects, and the Full QDNN is the optimized QDNN we use for all subsequent extractions.

Model	Algorithmic Error				Methodological Error				Precision				Accuracy			
	$\Re\mathcal{H}$	$\Re\mathcal{E}$	$\Re\tilde{\mathcal{H}}$	$DVCS$	$\Re\mathcal{H}$	$\Re\mathcal{E}$	$\Re\tilde{\mathcal{H}}$	$DVCS$	$\Re\mathcal{H}$	$\Re\mathcal{E}$	$\Re\tilde{\mathcal{H}}$	$DVCS$	$\Re\mathcal{H}$	$\Re\mathcal{E}$	$\Re\tilde{\mathcal{H}}$	$DVCS$
Basic	0.174	0.241	0.241	0.00227	0.0395	0.0482	0.0412	0.000208	0.454	0.652	1.02	0.00520	0.759	0.0330	0.0495	0.00259
1	0.135	0.169	0.170	0.00258	0.0405	0.0468	0.0367	0.000339	0.372	0.529	0.851	0.00638	0.765	0.0632	0.0351	0.00252
2	0.147	0.191	0.196	0.000559	0.0395	0.0471	0.0360	0.000153	0.416	0.573	0.870	0.00498	0.752	0.0389	0.0264	0.00255
3	0.137	0.177	0.173	0.00241	0.0404	0.0469	0.0373	0.000260	0.376	0.531	0.852	0.00533	0.764	0.0604	0.0321	0.00260
Full	0.127	0.161	0.175	0.000502	0.0408	0.0470	0.0356	0.000157	0.402	0.578	0.864	0.00511	0.773	0.0327	0.00018	0.00264

TABLE XIX: Results from the optimized CFF extraction from the real experimental data subset performed in Sec. VII. For each set of kinematics, the mean and standard deviation of the FQDNN-predicted CFFs are listed.

Set	k	Q^2	x_B	t	Mean $\text{Re}\mathcal{H}$	Std $\text{Re}\mathcal{H}$	Mean $\text{Re}\mathcal{E}$	Std $\text{Re}\mathcal{E}$	Mean $\text{Re}\tilde{\mathcal{H}}$	Std $\text{Re}\tilde{\mathcal{H}}$	Mean $DVCS$	Std $DVCS$
108	5.750	1.790	0.244	-0.110	-1.304	0.714	-1.604	0.798	-1.548	0.848	-0.0137	0.0200
109	5.750	1.790	0.244	-0.150	-0.222	0.498	-0.540	0.825	0.058	0.757	0.0201	0.0113
110	5.750	1.790	0.244	-0.200	-0.934	0.503	-0.962	0.544	-1.448	0.726	0.0080	0.0085
111	5.750	1.790	0.244	-0.260	-0.577	0.543	-0.724	0.635	-0.208	1.085	0.0196	0.0076
112	5.750	1.800	0.244	-0.340	-0.465	0.905	-0.731	0.912	0.160	0.836	0.0222	0.0080
113	5.750	1.800	0.244	-0.450	-0.508	1.640	-0.400	1.404	-0.240	0.596	0.0166	0.0090
114	5.750	2.120	0.244	-0.110	1.270	0.826	1.376	0.855	1.405	0.901	-0.0234	0.0170
115	5.750	2.120	0.245	-0.150	2.950	0.990	2.909	0.908	2.937	1.127	0.0406	0.0136
116	5.750	2.120	0.245	-0.200	4.590	1.532	3.880	1.371	3.496	1.437	0.0453	0.0176
117	5.750	2.120	0.245	-0.260	5.603	1.775	4.825	1.587	3.557	1.468	0.0573	0.0170
118	5.750	2.120	0.245	-0.340	9.494	3.111	8.464	2.769	5.397	2.212	0.0723	0.0223
119	5.750	2.120	0.245	-0.450	0.538	1.557	0.588	1.438	0.119	0.931	0.0193	0.0101
120	5.750	1.940	0.274	-0.110	-0.594	1.161	-0.973	1.988	-1.083	1.833	0.0261	0.0280
121	5.750	1.940	0.274	-0.150	-1.234	0.626	-1.707	0.754	-1.894	0.795	0.0022	0.0119
122	5.750	1.940	0.274	-0.200	-0.700	0.439	-1.177	0.575	-0.523	0.674	0.0028	0.0078
123	5.750	1.940	0.274	-0.260	-1.132	0.460	-1.286	0.491	-1.729	0.570	0.0091	0.0069
124	5.750	1.940	0.275	-0.340	-0.152	0.504	-0.218	0.573	0.392	1.135	0.0086	0.0052
125	5.750	1.940	0.275	-0.450	-0.159	0.756	-0.129	0.919	-0.305	0.613	0.0133	0.0040
126	5.750	2.350	0.274	-0.110	0.911	1.706	1.269	2.371	1.203	2.245	-0.0420	0.0366
127	5.750	2.350	0.275	-0.150	0.580	0.911	0.701	1.094	0.718	1.204	0.0038	0.0105
128	5.750	2.350	0.275	-0.200	1.874	0.899	1.975	0.874	2.159	1.023	0.0150	0.0073
129	5.750	2.350	0.275	-0.260	3.161	1.189	3.095	1.138	2.886	1.323	0.0288	0.0077
130	5.750	2.350	0.275	-0.340	3.104	1.320	2.424	1.122	1.522	0.858	0.0246	0.0067
131	5.750	2.350	0.275	-0.450	7.237	2.637	6.298	2.351	3.682	1.580	0.0340	0.0102
133	5.750	2.100	0.304	-0.150	-2.007	1.511	-3.181	2.303	-3.098	2.231	0.0263	0.0319
134	5.750	2.100	0.304	-0.200	-0.690	0.453	-1.249	0.698	-1.231	0.619	0.0040	0.0062
135	5.750	2.100	0.304	-0.260	-0.651	0.437	-0.938	0.567	-1.174	0.719	0.0058	0.0059
136	5.750	2.100	0.304	-0.340	-0.662	0.322	-0.802	0.368	-1.464	0.499	0.0053	0.0040
137	5.750	2.100	0.305	-0.450	-0.329	0.390	-0.368	0.424	-0.547	0.845	0.0116	0.0029
139	5.750	2.580	0.304	-0.150	-0.852	2.441	-1.130	3.231	-1.087	3.148	0.0128	0.0421
140	5.750	2.580	0.304	-0.200	0.094	0.545	0.143	0.847	0.085	0.918	-0.0003	0.0049
141	5.750	2.580	0.305	-0.260	2.103	0.771	2.269	0.740	2.566	0.799	0.0100	0.0039
142	5.750	2.580	0.305	-0.340	1.524	0.932	1.620	0.909	1.085	0.907	0.0106	0.0038
143	5.750	2.580	0.305	-0.450	2.056	1.553	1.510	1.189	0.790	0.741	0.0135	0.0042
145	5.750	2.230	0.335	-0.200	-0.086	0.381	-0.197	0.933	-0.271	1.036	-0.0060	0.0048
146	5.750	2.230	0.335	-0.260	-0.658	0.456	-1.031	0.669	-1.619	0.773	0.0080	0.0059
147	5.750	2.230	0.335	-0.340	-0.429	0.393	-0.548	0.484	-0.867	0.780	0.0086	0.0040
148	5.750	2.230	0.335	-0.450	-1.064	0.311	-1.210	0.338	-2.108	0.395	0.0044	0.0026
150	5.750	2.780	0.335	-0.200	-0.914	0.635	-1.603	0.866	-1.505	0.888	0.0026	0.0054
151	5.750	2.780	0.335	-0.260	-0.052	0.385	-0.081	0.768	-0.223	0.864	0.0015	0.0027
152	5.750	2.780	0.335	-0.340	1.135	0.615	1.442	0.658	1.700	0.760	0.0075	0.0022
153	5.750	2.780	0.335	-0.450	0.784	0.845	0.989	0.995	0.429	0.650	0.0060	0.0020
154	5.750	2.350	0.365	-0.200	-1.929	1.139	-5.204	2.382	-4.058	2.066	0.0097	0.0110
155	5.750	2.350	0.365	-0.260	-0.902	0.543	-1.813	0.936	-1.961	0.998	0.0047	0.0057
156	5.750	2.350	0.365	-0.340	-0.340	0.412	-0.507	0.591	-0.836	0.943	0.0061	0.0040
157	5.750	2.350	0.365	-0.450	-0.373	0.284	-0.462	0.343	-0.983	0.606	0.0036	0.0027
158	5.750	2.970	0.364	-0.200	-0.330	0.875	-0.857	2.353	-0.649	1.728	-0.0014	0.0055
159	5.750	2.970	0.365	-0.260	0.007	0.331	-0.015	0.970	0.083	1.067	0.0037	0.0026
160	5.750	2.970	0.365	-0.340	0.583	0.400	1.137	0.603	1.293	0.707	0.0021	0.0017
161	5.750	2.970	0.365	-0.450	0.976	0.391	1.283	0.444	1.943	0.444	0.0036	0.0011
163	5.750	2.480	0.400	-0.260	0.140	0.521	0.375	1.376	0.293	1.123	-0.0001	0.0047
164	5.750	2.480	0.399	-0.340	-0.193	0.524	-0.323	0.821	-0.434	1.061	0.0057	0.0045
165	5.750	2.480	0.399	-0.450	-0.699	0.312	-0.905	0.385	-1.481	0.574	0.0018	0.0024
166	5.750	3.120	0.391	-0.210	-1.311	1.796	-3.921	4.696	-2.405	3.127	0.0191	0.0134
167	5.750	3.180	0.399	-0.260	-1.064	0.742	-2.757	1.586	-2.147	1.324	0.0002	0.0038
168	5.750	3.180	0.400	-0.340	-0.347	0.273	-1.059	0.645	-1.434	0.731	0.0023	0.0015
169	5.750	3.180	0.400	-0.450	0.073	0.139	0.155	0.269	0.189	0.795	0.0032	0.0009
171	5.750	2.960	0.449	-0.340	0.248	0.424	0.757	1.164	0.549	0.867	0.0010	0.0027
172	5.750	3.050	0.461	-0.450	-0.114	0.186	-0.276	0.400	-0.411	0.521	0.0016	0.0009
173	5.750	3.500	0.430	-0.280	-1.382	1.844	-3.202	3.750	-2.327	2.896	-0.0006	0.0098
174	5.750	3.630	0.451	-0.340	-0.072	0.345	-0.256	1.167	-0.168	0.723	0.0006	0.0016
175	5.750	3.770	0.475	-0.450	0.108	0.174	0.279	0.440	0.275	0.405	0.0010	0.0006

-
- [1] K. Beer, D. Bondarenko, T. Farrelly, T. J. Osborne, R. Salzmann, D. Scheiermann, and R. Wolf, Training deep quantum neural networks, *Nat. Commun.* **11**, 808 (2020).
 - [2] A. V. Belitsky, D. Müller, and A. Kirchner, Theory of deeply virtual Compton scattering on the nucleon, *Nucl. Phys. B* **629**, 323 (2002).
 - [3] A. V. Belitsky and D. Müller, Refined analysis of photon leptonproduction off a spinless target, *Phys. Rev. D* **79**, 014017 (2009).
 - [4] A. V. Belitsky and D. Müller, Exclusive electroproduction revisited: Treating kinematical effects, *Phys. Rev. D* **82**, 074010 (2010).
 - [5] A. V. Belitsky, D. Müller, and Y. Ji, Compton scattering: From deeply virtual to quasi-real, *Nucl. Phys. B* **878**, 214 (2014).
 - [6] V. M. Braun, A. N. Manashov, D. Müller, and B. M. Pirnay, Deeply virtual Compton scattering to the twist-four accuracy: Impact of finite- t and target mass corrections, *Phys. Rev. D* **89**, 074022 (2014).
 - [7] Y. Guo, X. Ji, B. Kriesten, and K. Shiells, Twist-three cross-sections in deeply virtual Compton scattering, *J. High Energy Phys.* **2022**, 96.
 - [8] K. Kumeriški, D. Müller, and A. Schäferd, Neural network generated parametrizations of deeply virtual Compton form factors, *J. High Energy Phys.* **2011**, 73.
 - [9] H. Moutarde, P. Sznajder, and J. Wagner, Unbiased determination of DVCS compton form factors, *Eur. Phys. J. C* **79**, 614 (2019).
 - [10] B. D. Ripley, *Stochastic Simulation* (Wiley, New York, NY, USA, 1987).
 - [11] A. Bacchetta, U. D'Alesio, M. Diehl, and C. A. Miller, Single-spin asymmetries: The Trento conventions, *Phys. Rev. D* **70**, 117504 (2004).
 - [12] J. J. Kelly, Simple parametrization of nucleon form factors, *Phys. Rev. C* **70**, 068202 (2004).
 - [13] X. Ji, Deeply virtual Compton scattering, *Phys. Rev. D* **55**, 7114 (1997).
 - [14] X. Ji and J. Osborne, One-loop corrections and all order factorization in deeply virtual Compton scattering, *Phys. Rev. D* **58**, 094018 (1997).
 - [15] B. E. White, Factorization in deeply virtual Compton scattering: local OPE formalism and structure functions, *J. Phys. G* **28**, 203 (2001).
 - [16] M. Diehl, Generalized parton distributions, *Phys. Rep.* **388**, 41 (2003).
 - [17] V. Bertone, H. Dutrieux, C. Mezrag, H. Moutarde, and P. Sznajder, Deconvolution problem of deeply virtual Compton scattering, *Phys. Rev. D* **103**, 114019 (2021).
 - [18] D. Mueller, D. Robaschik, B. Geyer, F. Dittes, and J. Hořejši, Wave functions, evolution equations and evolution kernels from light ray operators of QCD, *Fortschr. Phys.* **42**, 101 (1994).
 - [19] V. Bergholm, J. Izaac, M. Schuld, C. Gogolin, S. Ahmed, V. Ajith, M. S. Alam, G. Alonso-Linaje, B. Akash-Narayanan, A. Asadi, *et al.*, PennyLane: Automatic differentiation of hybrid quantum-classical computations, *arXiv:1811.04968* (2018).
 - [20] K. Mitarai, M. Negoro, M. Kitagawa, and K. Fujii, Quantum circuit learning, *Phys. Rev. A* **98**, 032309 (2018).
 - [21] J. Biamonte, P. Wittek, N. Pancotti, P. Rebentrost, N. Wiebe, and S. Lloyd, Quantum machine learning, *Nature* **549**, 195 (2017).
 - [22] M. Schuld, I. Sinayskiy, and F. Petruccione, An introduction to quantum machine learning, *Contemp. Phys.* **56**, 172 (2015).
 - [23] V. Havlíček, A. D. Córcoles, K. Temme, A. W. Harrow, A. Kandala, J. M. Chow, and J. M. Gambetta, Supervised learning with quantum-enhanced feature spaces, *Nature* **567**, 209 (2019).
 - [24] M. Schuld and N. Killoran, Quantum machine learning in feature Hilbert spaces, *Phys. Rev. Lett* **122**, 040504 (2019).
 - [25] A. Abbas, D. Sutter, C. Zoufal, A. Lucchi, A. Figalli, and S. Woerner, The power of quantum neural networks, *Nat. Comput. Sci.* **1**, 403 (2021).
 - [26] S. Hochreiter, The vanishing gradient problem during learning recurrent neural nets and problem solutions, *Int. J. Uncertain. Fuzziness Knowl.-Based Syst.* **6**, 107 (1998).
 - [27] J. R. McClean, S. Boixo, V. N. Smelyanskiy, R. Babbush, and H. Neven, Barren plateaus in quantum neural network training landscapes, *Nat. Commun.* **9**, 4812 (2018).
 - [28] M. Cerezo, A. Sone, T. Volkoff, L. Cincio, and P. J. Coles, Cost function dependent barren plateaus in shallow parametrized quantum circuits, *Nat. Commun.* **12**, 1791 (2021).
 - [29] Y. Du, M.-H. Hsieh, T. Liu, and D. Tao, Expressive power of parametrized quantum circuits, *Phys. Rev. Research* **2**, 033125 (2020).
 - [30] C. Zoufal, A. Lucchi, and S. Woerner, Quantum generative adversarial networks for learning and loading random distributions, *npj Quantum Inf.* **5**, 103 (2019).
 - [31] M. A. Nielsen and I. L. Chuang, *Quantum Computation and Quantum Information* (Cambridge University Press, 2010).
 - [32] J. Preskill, Quantum computing in the NISQ era and beyond, *Quantum* **2**, 79 (2018).
 - [33] A. W. Harrow, A. Hassidim, and S. Lloyd, Quantum algorithm for linear systems of equations, *Phys. Rev. Lett.* **103**, 150502 (2009).
 - [34] M. Cerezo, A. Arrasmith, R. Babbush, S. C. Benjamin, S. Endo, K. Fujii, J. R. McClean, K. Mitarai, X. Yuan, L. Cincio, and P. J. Coles, Variational quantum algorithms, *Nat. Rev. Phys.* **3**, 625 (2021).
 - [35] E. Farhi and H. Neven, Classification with quantum neural networks on near term processors, *arXiv:1802.06002* (2018).
 - [36] M. Schuld, R. Sweke, and J. J. Meyer, Effect of data encoding on the expressive power of variational quantum-machine-learning models, *Phys. Rev. A* **103**, 032430 (2021).
 - [37] M. Schuld and F. Petruccione, *Machine Learning with Quantum Computers*, 2nd ed. (Springer Cham, 2021).
 - [38] R. O. Duda, P. E. Hart, and D. G. Stork, *Pattern Classification*, 2nd ed. (Wiley, 2001).
 - [39] I. Cong, S. Choi, and M. D. Lukin, Quantum convolutional neural networks, *Nat. Phys.* **15**, 1273 (2019).
 - [40] H.-Y. Huang, M. Broughton, M. Mohseni, R. Babbush, S. Boixo, H. Neven, and J. R. McClean, Power of data in quantum machine learning, *Nat. Commun.* **12**, 2631 (2021).

- [41] A. Senokosov, A. Sedykh, A. Sagingalieva, B. Kyriacou, and A. Melnikov, Quantum machine learning for image classification, *Mach. Learn.: Sci. Technol.* **5**, 015040 (2024).
- [42] A. Pesah, M. Cerezo, S. Wang, T. Volkoff, A. T. Sornborger, L. Cincio, and P. J. Coles, Absence of barren plateaus in quantum convolutional neural networks, *Phys. Rev. X* **11**, 041011 (2021).
- [43] D. Alvarez-Estevéz, Benchmarking quantum machine learning kernel training for classification tasks, *IEEE Trans. Quantum Eng.* (2025).
- [44] D. C. Montgomery, E. A. Peck, and G. G. Vining, *Introduction to Linear Regression Analysis*, 5th ed. (John Wiley & Sons, Hoboken, NJ, 2012).
- [45] R. Telgarsky, Dominant frequency extraction, *arXiv:1306.0103* (2013).
- [46] F. Shen and J. Liu, QFCNN: Quantum Fourier convolutional neural network, *arXiv:2106.10421* (2021).
- [47] S. Buczkowski, P. Hildgen, and L. Cartilier, Measurements of fractal dimension by box-counting: a critical analysis of data scatter, *Physica A* **252**, 23 (1998).
- [48] G. Verdon, J. Pye, and M. Broughton, Interpretable quantum advantage in neural sequence learning, *PRX Quantum* **4**, 020338 (2023).
- [49] A. Kraskov, H. Stögbauer, and P. Grassberger, Estimating mutual information, *Phys. Rev. E* **69**, 066138 (2004).
- [50] D. Basilewitsch, J. F. Bravo, C. Tutschku, and F. Struckmeier, Quantum neural networks in practice: A comparative study with classical models from standard data sets to industrial images, *arXiv:2411.19276* (2025).
- [51] P. Stoica and R. Moses, *Spectral Analysis of Signals* (Pearson Prentice Hall, 2005).
- [52] S. Y.-C. Chen, T.-C. Wei, C. Zhang, H. Yu, and S. Yoo, Quantum convolutional neural networks for high energy physics data analysis, *Phys. Rev. Research* **4**, 013231 (2022).
- [53] F. Georges *et al.*, Deeply virtual Compton scattering cross section at high Bjorken x_B , *Phys. Rev. Lett.* **128**, 252002 (2022).
- [54] M. Defurne *et al.*, A glimpse of gluons through deeply virtual Compton scattering on the proton, *Nat. Commun.* **8**, 1408 (2017).
- [55] M. Defurne *et al.*, E00-110 experiment at Jefferson Lab Hall A: Deeply virtual Compton scattering off the proton at 6 GeV, *Phys. Rev. C* **92**, 055202 (2015).
- [56] H. S. Jo and *et al.* (CLAS Collaboration), Cross sections for the exclusive photon electroproduction on the proton and generalized parton distributions, *Phys. Rev. Lett.* **115**, 212003 (2015).
- [57] A. Paszke, S. Gross, F. Massa, A. Lerer, J. Bradbury, G. Chanan, T. Killeen, Z. Lin, N. Gimelshein, L. Antiga, *et al.*, Pytorch: An imperative style, high-performance deep learning library, *Adv. Neural Inf. Process. Syst.* **32** (2019).
- [58] X. Glorot and Y. Bengio, Understanding the difficulty of training deep feedforward neural networks, *Proceedings of the Thirteenth International Conference on Artificial Intelligence and Statistics* **9**, 249 (2010).
- [59] K. Kumerički and D. Müller, Description and interpretation of DVCS measurements, *EPJ Web Conf.* **112**, 01012 (2016).
- [60] K. Kumerički and D. Müller, Deeply virtual Compton scattering at small x_B and the access to the GPD H , *Nucl. Phys. B* **841**, 1 (2010).
- [61] K. Kumerički, D. Müller, and M. Murray, HERMES impact for the access of Compton form factors, *Phys. Part. Nucl.* **45**, 723 (2014).
- [62] C. M. Camacho *et al.*, Scaling tests of the cross section for deeply virtual Compton scattering, *Phys. Rev. Lett.* **97**, 262002 (2006).
- [63] F. X. Girod *et al.*, Measurement of deeply virtual Compton scattering beam-spin asymmetries, *Phys. Rev. Lett.* **100**, 162002 (2008).
- [64] G. Gavalian *et al.*, Beam spin asymmetries in deeply virtual Compton scattering with CLAS at 4.8 GeV, *Phys. Rev. C* **80**, 035206 (2009).
- [65] U. S. P. Group, QDNN-CFF: Quantum deep neural network extraction of Compton form factors, <https://github.com/uva-spin/QDNN-CFF> (2025), uploaded: 2025-07-29.